This is the accepted manuscript made available via CHORUS. The article has been published as:

# Semiclassical control theory of coherent anti-Stokes Raman scattering maximizing vibrational coherence for remote detection

J. Chathanathil, G. Liu, and S. A. Malinovskaya

Phys. Rev. A **104**, 043701 — Published 5 October 2021

DOI: 10.1103/PhysRevA.104.043701

# A semi-classical control theory of Coherent Anti-Stokes Raman Scattering (CARS) maximizing vibrational coherence for remote detection

J. Chathanathil, G. Liu, S. A. Malinovskaya

*Department of Physics*

*Stevens Institute of Technology*

*Hoboken, NJ 07030, USA*

(Dated: September 20, 2021)

## Abstract

A semiclassical theory that describes a generation of the anti-Stokes CARS signal is presented that maximizes vibrational coherence in a mode predetermined by the pump, the Stokes and the probe chirped pulse trains and takes into account the field propagation effects in a cloud of molecules. The built-up of the anti-Stokes signal which may be used as a molecular signature in the backward CARS signal is demonstrated numerically. The theory is based on the solution of the coupled Maxwell's and the Liouville von Neumann equations, and focuses on the quantum effects induced in the target molecules by the control pulse trains. A deep Convolutional Neural Network technique is implemented to evaluate time-dependent phase characteristics of the control fields. The effect of decoherence induced by spontaneous decay and collisional dephasing is examined.

## I. INTRODUCTION

Coherent anti-Stokes Raman scattering (CARS) belongs to the frontiers of non-linear optics methods suited for imaging, sensing and detection without labeling or destruction [1]. The implementation of ultrafast pulses in the stimulated Raman spectroscopy in general and CARS in particular brings advantages of the high peak power, the three-dimensional spacial resolution, and the femtosecond time resolution to monitor vibrational dynamics [2–12]. Femtosecond CARS has been widely used and nowadays advances toward solving tasks related to a single molecule spectroscopy, molecular specific imaging, sensing traces of molecules and remote detection [13–18]. Success in these areas depends on a high level of chemical sensitivity and specificity, the signal to noise ratio, and the CARS signal intensity. Because the Raman fields' evolution is proportional to the macroscopic induced polarization [19], which in its turn is proportional to a microscopic quantum property of the material, quantum coherence, crafting ultrafast laser pulses to generate the maximum coherence in the target molecules is the root to impact the molecular-specific response and to significantly enhance the signal. To date, there has been a number of methods developed to achieve the maximum coherence leading to the enhancement of the signal from predetermined vibrational modes in CARS using the shaped ultrafast pulses. Among pioneering works including those for remote detection are [20–22], [23, 24] and [25–32] proposing different phase shaping of the ultrafast pulses. Other notable works are the multiplex CARS using a combination of a narrow-band chirped pump and probe and a transform-limited broadband Stokes pulse [33] and a proposal of double parabolic phase functions in the stimulated Raman scattering (SRS) [34].

In this paper, we present a semiclassical theory of a generation of the anti-Stokes signal by creating the maximum vibrational coherence in a predetermined mode with the pump, the Stokes and the probe chirped pulse trains in the four-wave mixing in CARS and take into account the field propagation effect in a cloud of molecules. The motivation is to demonstrate the built-up of the anti-Stokes signal which may be used as a molecular signature in the backward CARS signal. The theory is based on the solution of the coupled sets of Maxwell's and the Liouville von Neumann equations and focuses on the quantum effects induced in the target molecules by the shaped laser pulse trains. We analyze the enhancement of the backscattered anti-Stokes signal upon multiple scattering of radiation from the target

molecules, which modifies propagating fields. We examine the impact of decoherence induced by spontaneous decay and collisional dephasing. We demonstrate that decoherence due to spontaneous decay can be mitigated by applying the control pulse trains with the train period close to the decay time.

The novelty of the study is in the demonstration of the built-up of coherent anti-Stokes signal as a result of controllability of vibrational coherence in the target molecules upon four chirped pulse trains propagation subject to multiple scattering events, in utilizing the pulse train properties to mitigate decoherence and in implementing the Deep Convolution Network approach to evaluate the phase of the propagating fields, which provides with the information about the relative phase change between the pump, the Stokes, the probe and the anti-Stokes pulses.

As a case study we use the methanol vapor. Methanol molecules have Raman active symmetric 2837 $cm^{-1}$ (85.05 THz) and asymmetric 2942 $cm^{-1}$ (88.20 THz) stretch modes. These values are within the range of molecular group vibrations in various biochemical species, which span from 2800 to 3100 $cm^{-1}$ making the methanol a suitable choice as a surrogate molecule for non-hazardous experiments in the lab. Thus, the results of methanol studies would be useful for the development of remote detection schemes as well as for the environmental analyses.

Various setups are available to perform CARS experiments satisfying the phase-matching conditions to separate the directional anti-Stokes signal from the incident fields. However for particles having a size comparable to the wavelength, the phase-mismatched factor is small and it was shown that the non-phase-matched CARS can provide an effective method to probe complex molecules [22, 35]. For methanol, the ratio $4\pi\rho_0/\lambda \ll 1$, where $\rho_0 \sim 10^{-10}m$ is the target molecule diameter; it relaxes the phase-matching condition and permits consideration of the collinear copropagating fields configuration.

The paper is organized as follows. In Section II, a theoretical framework is formulated. Section III discusses the machine learning approach for a numerical analysis of the phase of the propagating fields. Section IV contains the numerical results for the methanol and a discussion. The paper concludes with a Summary.

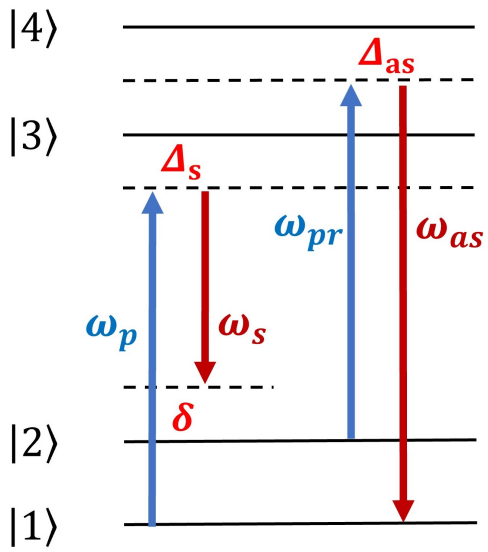


FIG. 1: Schematic of CARS: the pump ($\omega_p$) and the Stokes ($\omega_s$) fields interact with the ground vibrational state $|1\rangle$ and the excited vibrational $|2\rangle$ state of the ground electronic state in the target molecule to create a superposition state with coherence $\rho_{12}$. The probe ($\omega_{pr}$) field interacts with this superposition state to generate anti-Stokes field at frequency $\omega_{as}$. Parameters $\Delta_s$ and $\Delta_{as}$ are the one-photon detunings, and $\delta$ is the two-photon detuning.

## II. THEORETICAL FRAMEWORK

### A. Maxwell - Liouville von Neumann formalism

CARS is a third order nonlinear process in which three beams, the pump, the Stokes and the probe, at frequencies $\omega_p$, $\omega_s$ and $\omega_{pr}$ respectively, interact with the electronic vibrational - vibronic - states of the target molecules to generate the anti-Stokes field at frequency $\omega_{as} = \omega_p + \omega_{pr} - \omega_s$, Fig(1). In our control scheme, we use linearly chirped pulse trains which read

$$E_i(t) = \sum_{k=0}^{N-1} E_{i0} exp\{-\frac{(t - t_c - kT)^2}{2\tau^2}\} \cos\{\omega_{i0}(t - t_c - kT) + \alpha_i \frac{(t - t_c - kT)^2}{2}\}. \quad (1)$$

Here $T$ is the pulse train period, $t_c$ is the central time when the peak value of the Gaussian field envelope is $E_0$, $\tau$ is the chirp-dependent pulse duration, $\omega_{i0}$ is the carrier frequency, and $\alpha_i$, $i = p, s, pr$, is the linear chirp rate of an individual pump, Stokes and probe pulse in the respective pulse train. The values of $\alpha_i$ are chosen in accordance with the control

scheme, which implies $\alpha_s = -\alpha_p$ and $\alpha_{pr} = \alpha_s - \alpha_p$ for $t \leq t_c$; and $\alpha_s = \alpha_p$ and $\alpha_{pr} = 0$ for $t > t_c$ [36]. Such chirped pulses induce the maximum coherence between vibronic states in the target molecules via adiabatic passage provided the two-photon detuning $\delta = 0$. Any slightly different vibrational mode not satisfying the two-photon resonance condition, $\delta \neq 0$, is suppressed. The selectivity of the mode excitation is determined by the condition $\tau\delta \geq 1$. The chirped pulse duration $\tau$ relates to the transform-limited pulse duration $\tau_0$ as $\tau = \tau_0(1 + \alpha'^2/\tau_0^4)^{1/2}$, and the temporal ($\alpha$) and the spectral ($\alpha'$) chirps relate as $\alpha = \alpha'\tau_0^{-4}/(1 + \alpha'^2/\tau_0^4)$.

The matrix Hamiltonian written in the interaction representation and in the rotating wave approximation (RWA) reads

$$H = \frac{\hbar}{2}\begin{pmatrix} 0 & 0 & \Omega_{p_0}(t)e^{i\Delta_s t + i\frac{\alpha_p}{2}t^2} & \Omega_{as_0}(t)e^{i\Delta_{as}t} \\ 0 & 0 & \Omega_{s_0}(t)e^{i\Delta_s t + i\frac{\alpha_s}{2}t^2} & \Omega_{pr_0}(t)e^{i\Delta_{as}t + i\frac{\alpha_{pr}}{2}t^2} \\ \Omega^*_{p_0}(t)e^{-i\Delta_s t - i\frac{\alpha_p}{2}t^2} & \Omega^*_{s_0}(t)e^{-i\Delta_s t - i\frac{\alpha_s}{2}t^2} & 0 & 0 \\ \Omega^*_{as_0}(t)e^{-i\Delta_{as}t} & \Omega^*_{pr_0}(t)e^{-i\Delta_{as}t - i\frac{\alpha_{pr}}{2}t^2} & 0 & 0 \end{pmatrix} \quad (2)$$

Here $\Omega_{p_0}(t) = -\mu_{31}/\hbar E_{p_0}(t)$, $\Omega_{s_0}(t) = -\mu_{32}/\hbar E_{s_0}(t)$, $\Omega_{pr_0}(t) = -\mu_{42}/\hbar E_{pr_0}(t)$, $\Omega_{as_0}(t) = -\mu_{41}/\hbar E_{as_0}(t)$ are the Rabi frequencies of respective fields, $\mu_{ij}$ is a dipole moment, $\Delta_s$ and $\Delta_{as}$ are the one-photon detunings on transitions $|1\rangle \rightarrow |3\rangle$ and $|1\rangle \rightarrow |4\rangle$ respectively.

To account for the propagation effects in the scattering process, we combine the Liouville von Neumann equation for the states with Maxwell's equations for the fields. The displacement current is determined as $D = \epsilon_0 E + P$, where P is the expectation value of the induced dipole moment and $\epsilon_0$ is the permittivity of free space. The effects arising from magnetization are neglected giving $B = \mu_0 H$, where $\mu_0$ is permeability of free space. The wave equation for a field propagating in the $\hat{z}$ direction and having polarization in the XY plane reads:

$$\left(\frac{\partial}{\partial z} + \frac{1}{c}\frac{\partial}{\partial t}\right)\left(-\frac{\partial}{\partial z} + \frac{1}{c}\frac{\partial}{\partial t}\right)E = -\mu_0\frac{\partial^2 P}{\partial t^2} \quad (3)$$

Assuming the field is $E(z,t) = \frac{1}{2}(E_0(z,t)e^{-i[\omega t - kz - \phi(z,t)]} + c.c)$ and considering $E_0(z,t)$ and $\phi(z,t)$ as slowly varying functions of position and time, Eq.(3) can be written as:

$$-2k\left(\frac{\partial E_0(z,t)}{\partial z} + \frac{1}{c}\frac{\partial E_0(z,t)}{\partial t}\right)\sin\left(\omega t - kz - \phi(z,t)\right) = -\mu_0\frac{\partial^2}{\partial t^2}P(z,t) \quad (4)$$

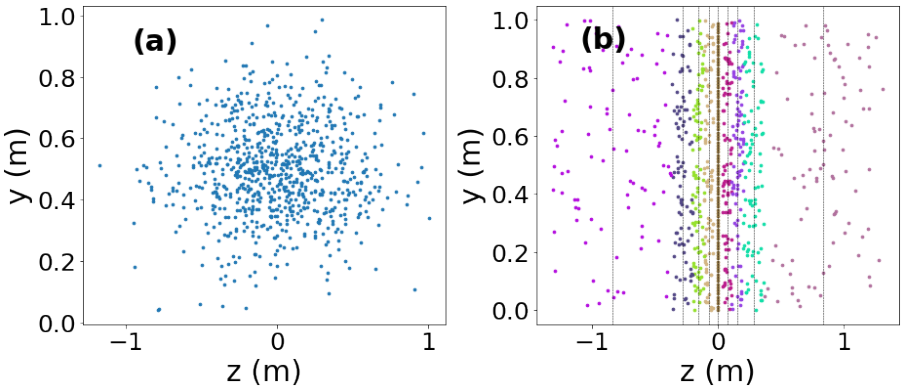


FIG. 2: The Gaussian distribution of the target molecules in (a) based on the density of molecules and in (b) is converted into multi-layer model; molecules are given different colors to distinguish the layers. Each layer in the multi-layer model is characterized by the fractional number density $\eta$ and a distance to it's adjacent layer $(\Delta z)_\eta$. If $N_s$ is the number of the target molecules and $N$ is the number of total molecules associated with the layer, the fractional number density of that layer is defined as $\eta = N_s/N$. The distance between the adjacent layers $(\Delta z)_\eta$ changes according to the Gaussian distribution of molecules. The incoming pulses pass through a series of scattering events with the target molecules within each layer to produce a detectable backscattered CARS signal.

Substituting $P(z,t) = \frac{1}{2}(P_0(z,t)e^{-i[\omega t - kz - \phi(z,t)]} + c.c)$ in the RHS, Eq.(3) becomes:

$$-2k(\frac{\partial E_0(z,t)}{\partial z} + \frac{1}{c}\frac{\partial E_0(z,t)}{\partial t}) = \mu_0\omega^2 Im\left[P_0(z,t)\right]. \tag{5}$$

In quantum theory, the macroscopic polarization P is given by the expectation value of the electric dipole moment $\hat{\mu}$; $\langle P(z,t)\rangle = N_s Tr\{\langle\rho(z,t)\cdot\mu\rangle\}$, where $N_s$ is the atomic density of the target molecules. Applied to the four-level system of CARS, the four components of P can written as: $P_{0p}(z,t) = N_s\mu_{13}\rho_{13}(z,t)$, $P_{0s}(z,t) = N_s\mu_{23}\rho_{23}(z,t)$, $P_{0pr}(z,t) = N_s\mu_{24}\rho_{24}(z,t)$, and $P_{0as}(z,t) = N_s\mu_{14}\rho_{14}(z,t)$. Eliminating the space component by substituting $\frac{\partial}{\partial z} = \frac{1}{c}\frac{\partial}{\partial t}$ and using these expressions of polarizations, Eq.(5) casts into

$$\frac{1}{c}\frac{\partial E_q}{\partial t} = -N_s\mu_0\mu_{ij}\frac{E_q(t)}{\hbar}\,\mathrm{Im}\{\rho_{ij}\} \tag{6}$$

where $q = p, s, pr, as$ and $i, j$ are the indexes of the states involved in the respective transitions.

The density matrix elements $\rho_{ij}$ are found from the Liouville von Neumann equation $i\hbar\dot{\rho} = [H, \rho]$ with the Hamiltonian from Eq.(2). After applying the rotation wave approximation and the adiabatic elimination of the excited states assuming that $\dot{\rho}_{13}, \dot{\rho}_{14}, \dot{\rho}_{23}, \dot{\rho}_{24}, \dot{\rho}_{34} \approx 0,\ \rho_{34} \approx 0,\ \rho_{33}, \rho_{44} \ll \rho_{11}, \rho_{22}$ and $\dot{\rho}_{33}, \dot{\rho}_{44} \approx 0$, and using the control condition on the chirp parameters $\alpha_s - \alpha_p = \alpha_{pr}$, the density matrix elements $\rho_{13}, \rho_{23}, \rho_{14}, \rho_{24}$ read in terms of $\rho_{11}, \rho_{22}$ and $\rho_{12}$ in the field interaction representation as follows

$$\begin{aligned}
\rho_{13} &= \frac{1}{2(\Delta_s + \alpha_p t)}\Omega_{p0}(t)\rho_{11} + \frac{1}{2(\Delta_s + \alpha_p t)}\Omega_{s0}(t)\rho_{12} \\
\rho_{23} &= \frac{1}{2(\Delta_s + \alpha_s t)}\Omega_{s0}(t)\rho_{22} + \frac{1}{2(\Delta_s + \alpha_s t)}\Omega_{p0}(t)\rho_{21} \\
\rho_{14} &= \frac{1}{2\Delta_{as}}\Omega_{as0}(t)\rho_{11} + \frac{1}{2\Delta_{as}}\Omega_{pr0}(t)\rho_{12} \\
\rho_{24} &= \frac{1}{2(\Delta_{as} + \alpha_{pr} t)}\Omega_{pr0}(t)\rho_{22} + \frac{1}{2(\Delta_{as} + \alpha_{pr} t)}\Omega_{as0}(t)\rho_{21}
\end{aligned} \tag{7}$$

The details of the derivation of Eqs.(7) are presented in Appendix A. Further, substituting Eq.(7) into Eq.(6) and rewriting the equations in terms of Rabi frequencies lead to the following Maxwell's equations:

$$\begin{aligned}
\frac{\partial \Omega_{p0}}{\partial t} &= c\frac{\partial \Omega_{p0}}{\partial z} = -\frac{\eta}{2(\Delta_s + \alpha_p t)}\kappa_{13}\omega_p \Omega_{s0}(t)\,\mathrm{Im}[\rho_{12}] \\
\frac{\partial \Omega_{s0}}{\partial t} &= c\frac{\partial \Omega_{s0}}{\partial z} = \frac{\eta}{2(\Delta_s + \alpha_s t)}\kappa_{23}\omega_s \Omega_{p0}(t)\,\mathrm{Im}[\rho_{12}] \\
\frac{\partial \Omega_{pr0}}{\partial t} &= c\frac{\partial \Omega_{pr0}}{\partial z} = \frac{\eta}{2(\Delta_{as} + \alpha_{pr} t)}\kappa_{24}\omega_{pr} \Omega_{as0}(t)\,\mathrm{Im}[\rho_{12}] \\
\frac{\partial \Omega_{as0}}{\partial t} &= c\frac{\partial \Omega_{as0}}{\partial z} = -\frac{\eta}{2(\Delta_{as})}\kappa_{14}\omega_{as} \Omega_{pr0}(t)\,\mathrm{Im}[\rho_{12}].
\end{aligned} \tag{8}$$

Here $\kappa_{ij} = N\mu_0\mu_{ij}^2 c^2/(3\hbar)$, N is the number density of molecules given by $N_A/V_0$ under the ideal gas conditions, where $N_A$ is the Avogadro's Number, $V_0$ is the molar volume, and $\eta$ is the fractional number density which will be described in detail in the next section. The factor 1/3 comes from the averaging over all orientations of the molecular dipole $\langle \mu_x \mu_y \rangle = \langle \mu_x \mu_z \rangle = \langle \mu_y \mu_z \rangle = 0$ and $\langle \mu_j \rangle = (1/3)\mu^2, j = x, y, z$ [37]. Considering dipole moment of methanol $\mu_{ij} = 1.70D$, the constant $\kappa_{ij}$ is found to be $3.636 \times 10^{-3}[\omega_{21}]$.

The Eqs.(8) coupled with the multi-layer model described below are numerically solved using the transform-limited and the control pulse trains to find the scattered anti-Stokes signal. Note, that the right side of Eqs.(8), which describes the induced polarization in the target molecules, depends only on the imaginary part of coherence $\rho_{21}$ out of all density

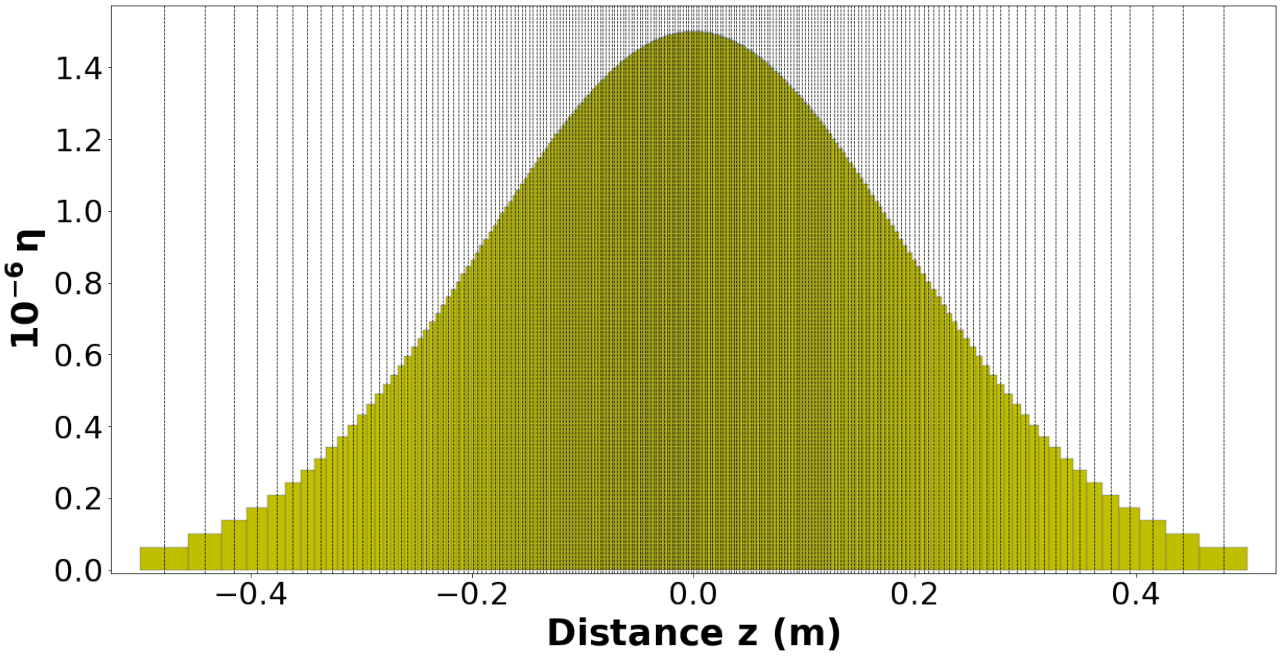


FIG. 3: An example of the multi-layer model of a molecular distribution for the width of the Gaussian distribution in Eq.(11) of the target molecules $\sigma = 0.19$ m. Here, each of 200 vertical lines represents the location of the scattering event and the scattering layers become more dense as the density peaks at the center.

matrix elements. Thus, the maximum value of this coherence provides the optimal amplitude of the scattered signal.

To analyze the impact of decoherence due to spontaneous decay and collisional dephasing of molecules, the Liouville von Neumann equations are augmented by the relaxation terms. Spontaneous decay from state $|i\rangle$ to state $|j\rangle$ is denoted by $\gamma_{ij}$, while collisional dephasing between states $|i\rangle$ and $|j\rangle$ is denoted by $\Gamma_{ij}$. Spontaneous decay impacts state populations and coherence via the diagonal and off-diagonal reduced density matrix elements respectively, while collisional dephasing assumed to be weak enough not to change state populations but to cause dipole phase interruption via off-diagonal reduced density matrix elements. Vibrational energy relaxation [38, 39] within the ground electronic state is accounted through parameter $\gamma_{21}$. We neglect vibrational energy relaxation within the excited electronic state since the respective vibrational states $|3\rangle$ and $|4\rangle$ are negligibly populated during dynamics. Vibrational energy relaxation is an important topic in chemical physics, since it relates to fundamental reaction processes [40, 41], conformational changes

[42] or spectroscopic measurements [43, 44], and its understanding is the first step toward controlling these phenomena.

$$
\begin{aligned}
\dot{\rho}_{11} &= -i/\hbar[H,\rho]_{11} + \gamma_{21}\rho_{22} + \gamma_{31}\rho_{33} + \gamma_{41}\rho_{44} \\
\dot{\rho}_{12} &= -i/\hbar[H,\rho]_{12} - (\gamma_{21}/2 + \Gamma_{21})\rho_{12} \\
\dot{\rho}_{13} &= -i/\hbar[H,\rho]_{13} - (\gamma_{31}/2 + \gamma_{32}/2 + \gamma_{21}/2 + \gamma_{41}/2 + \Gamma_{31})\rho_{13} \\
\dot{\rho}_{14} &= -i/\hbar[H,\rho]_{14} - (\gamma_{41}/2 + \gamma_{42}/2 + \gamma_{21}/2 + \gamma_{31}/2 + \Gamma_{41})\rho_{14} \\
\dot{\rho}_{22} &= -i/\hbar[H,\rho]_{22} - \gamma_{21}\rho_{22} + \gamma_{32}\rho_{33} + \gamma_{42}\rho_{44} \\
\dot{\rho}_{23} &= -i/\hbar[H,\rho]_{23} - (\gamma_{31}/2 + \gamma_{32}/2 + \gamma_{21}/2 + \gamma_{42}/2 + \Gamma_{32})\rho_{23} \\
\dot{\rho}_{24} &= -i/\hbar[H,\rho]_{24} - (\gamma_{41}/2 + \gamma_{42}/2 + \gamma_{21}/2 + \gamma_{23}/2 + \Gamma_{42})\rho_{24} \\
\dot{\rho}_{33} &= -i/\hbar[H,\rho]_{33} - (\gamma_{31} + \gamma_{32})\rho_{33} \\
\dot{\rho}_{34} &= -i/\hbar[H,\rho]_{34} - \Gamma_{43}\rho_{34} \\
\dot{\rho}_{44} &= -i/\hbar[H,\rho]_{44} - (\gamma_{41} + \gamma_{42})\rho_{44}.
\end{aligned}
\tag{9}
$$

### B. The target molecules distribution

We consider the target molecules as a cluster of molecules with its center located a large distance away from the source and its density following the Gaussian distribution. We introduce a multi-layer model to analyze the propagation and scattering of the pump, Stokes, probe and anti-Stokes pulses through this spatial distribution of molecules. The model mimics the distribution of molecules in the air and allows us to solve the propagation and scattering tasks in an elegant and simple way. In this model, each layer is characterized by the fractional number density $\eta$ and a distance to it adjacent layer $(\Delta z)_\eta$. The distance between the layers changes according to the Gaussian distribution of molecules. If $N_s$ is the number of the target molecules and $N$ is the number of total molecules associated with the layer, the fractional number density of that layer is defined as $\eta = N_s/N$. Suppose all target molecules in the central layer are arranged vertically next to each other with no background molecules between them, then the area occupied by these molecules is $S = \pi(d/2)^2 N_s$ giving $N_s = 4S/\pi d^2$, where $d$ is an approximate diameter of the target molecule. If $(\Delta z)_\eta$ is the width of this layer, the total number of molecules $N$ is $(S(\Delta z)_\eta/V_0)N_A$, where $V_0$ is the

molar volume and $N_A$ is the Avogadro's number. This gives

$$\eta = \frac{N_s}{N} = \frac{\frac{4S}{\pi d^2}}{(\frac{S(\Delta z)_\eta}{V_0})N_A} = \frac{4V_0}{\pi d^2 (\Delta z)_\eta N_A}. \tag{10}$$

We consider $N_s$ be constant within each layer. Now, we take $N = N_s$ for the central layer and calculate its width. For any subsequent layer the total number of molecules is different. Given $N_s$, the increase in the layer width by $\Delta z_\eta$ increases the layers volume and, thus, decreases the target's density by the factor $(1 + \Delta z_\eta/\Delta z_0)$. The width of each sequential layer is calculated using Eq.(10). Consider that the density changes as per the Gaussian distribution function having the full width at the half maximum (FWHM) $\sigma$ and its maximum value at the center $z_0$ of the cluster of molecules as

$$\eta = \frac{N_s V_0}{S N_A \sqrt{2\pi}\sigma} e^{-(z-z_0)^2/(2\sigma^2)}. \tag{11}$$

The maximum density $\eta_0$ of the central layer is found by substituting $z = z_0$ in Eq.(11). This value of $\eta$ is then substituted in the Eq.(10) to find the width of the central layer $(\Delta z)_\eta = (\Delta z)_0$. Once we find the width of the central layer, the $\eta$ of the adjacent layer is found by substituting the new value of $z$, $z_0 + (\Delta z)_\eta$, in Eq.(11). This process is repeated to find the entire density distribution of the cluster of molecules. The distance between scattering layers $(\Delta z)_\eta$ increases towards both ends of the distribution. So we converted the three dimensional cluster of molecules into a set of two-dimensional layers of molecules. Fig.(3) shows a set of layers, the distance between them and the density associated with each layer. In numerical calculations, we consider $\sigma = 0.2m$ with its center 1 km away from the source, which together with $\eta_0$ determines the total number of layers to be equal to 199.

### C. Propagation through atmosphere

For a completeness of the picture, taking into account the effects of atmosphere as pulses propagate through the molecular distribution is needed. The propagation of femtosecond pulses through the atmosphere under various air conditions has been broadly investigated, e.g. [45, 46]. Various effects during the propagation including the dispersion and the non-linear self-focusing are not within the scope of this paper. We use Beer's law under the ideal conditions to account for the change in the amplitude of the pulses as they propagate through

the atmosphere [47]. Assuming there is no turbulence and the air is homogeneous, the intensity of the pulse trains attenuate exponentially due to scattering and absorption as they propagate. The intensity $I$ as a function of the distance $z$ can be written as $I(z) = I_0 e^{-\beta_e z}$, where $\beta_e$ is the extinction coefficient that contains factors of both scattering and absorption. We use the clear air atmospheric coefficient of 0.55 $km^{-1}$ in numerical calculations [48] shown in Section IV.

## III. A DEEP NEURAL NETWORK FOR EVALUATION OF THE PHASE OF THE FIELDS SCATTERED FROM THE TARGET MOLECULES

To investigate the controllability of population dynamics and vibrational coherence in the target molecules by propagating electromagnetic fields we need to know the key fields' parameters evolution after each scattering event. This allows us to accurately calculate the quantum coherence and the induced polarization at the sequential steps of numerical calculation. In the case of using the chirped pulse control scheme within the multi-layer model of molecule distribution, the Maxwell - Liouville von Neumann equations alter the initial, pre-determined phase of the incident pulses impacting the response of the target molecules. Thus, extracting the analytical phase from the numerical solutions of Eqs.(8) and verifying that the chirping scheme is applied to each scattering event becomes an extremely important task for evaluating the response from the quantum system. To accomplish this goal, we developed a mechanism for classifying different kinds of pulses from the numerical data, based on their chirping and extracting the chirp parameters from these classified pulses using a machine learning technique [49, 50]. This approach of extracting the information about the phase of the pulses from the numerical grid and obtaining an accurate value of the chirp parameters is principally novel and may have a wide range of applications in the quantum control and spectroscopy.

The machine learning model we created is the deep Convolutional Neural Network (CNN). A CNN is built to classify a given pulse into one of three kinds: linear, quadratic and the chirp shape according to our control scheme $\alpha_s = -\alpha_p$ and $\alpha_{pr} = \alpha_s - \alpha_p$ for $t \leq t_c$; and $\alpha_s = \alpha_p$ and $\alpha_{pr} = 0$ for $t > t_c$. Another CNN is built to do the regression work, it calculates the parameters of the fields and shares a similar structure as the classification neural network. The structure will be discussed later in Appendix B.

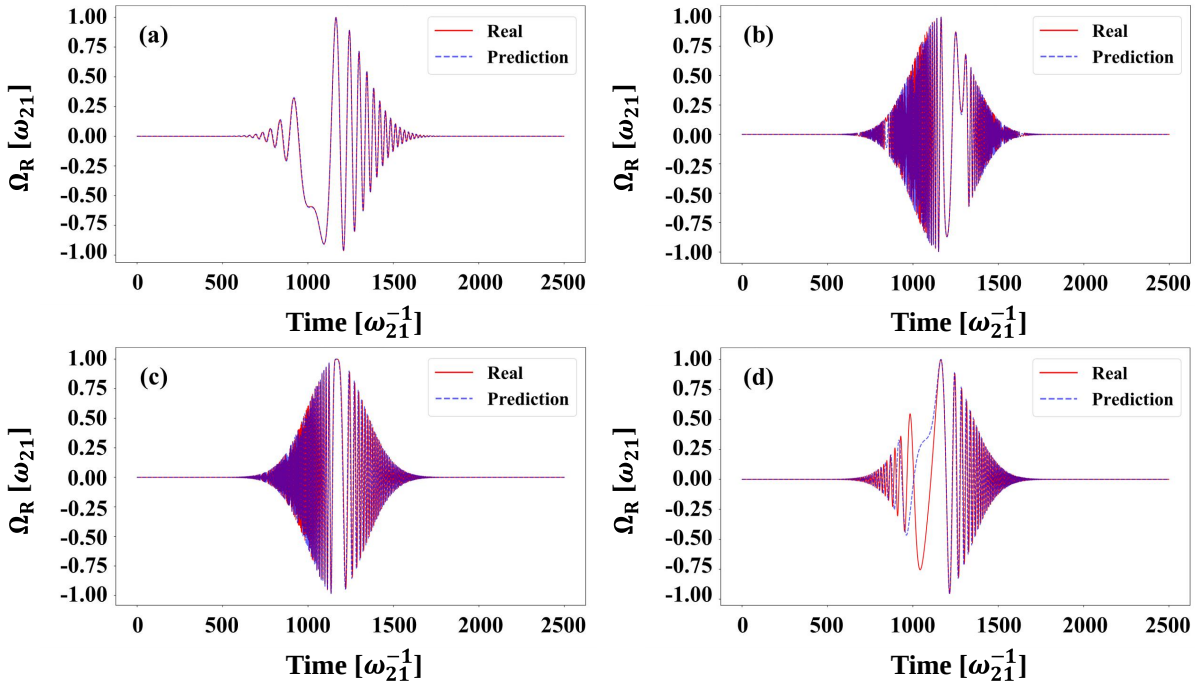


FIG. 4: Different shapes of the phase of the field obtained numerically (solid line) and using the deep convolution neural network model (dashed line) with different types of the phase of the input pulse: (a) Linear chirp, $\phi(t) = a_1 t + a_2 t^2$; (b) Quadratic dependence of the phase on time having $a_2 < 0$ in $\phi(t) = a_1 t + a_2 t^2 + a_3 t^3$; (c) 'Roof' chirp having positive chirp rate for the first and negative chirp rate for the second part of the pulse [36], $\phi(t) = a_1 t + \tilde{a}_2 t^2$ for $t \leq 0$, and $\phi(t) = a_1 t + \widetilde{\tilde{a}}_2 t^2$ for $t > 0$; (d) Quadratic dependence of the phase on time having $a_2 > 0$ in $\phi(t) = a_1 t + a_2 t^2 + a_3 t^3$. The values of parameters are printed in the titles of the pictures. Note that there is no discrepancy in determination of the kind of the phase, only parameters have rare errors.

Of principle importance for studying the phase of the numerical pulses is the availability of training data. Massive training data is a necessary requirement for deep learning training to concur a problem [51]. Since it is difficult to collect thousands of actual data from the experiments, we created a program that generated the scattered laser pulses randomly based on an arbitrary laser pulse model

$$E(t) = E_0 e^{-\frac{t^2}{2\tau^2}} \cos[\omega_L t + M(t)]. \tag{12}$$

Here $\tau$ is a single pulse duration, $E_0$ is the peak value of the field having the Gaussian envelope, and $\omega_L t + M(t)$ is the phase of the field having the modulation $M(t)$, which is

the key to quantum control. A different parity of the phase modulation leads to different control scenarios [52, 53]. Here we present $M(t)$ as an expansion in the Taylor series

$$M(t) = a_0 + a_1 t^1 + a_2 t^2 + a_3 t^3 + ... \tag{13}$$

Since in most cases the higher orders have a very limited contribution, we created data for three kinds of the phase using terms up to the third power in time: 'The Linear', which is determined by two parameters: the carrier frequency ($a_1$) and the linear chirp ($a_2$), then the field phase reads $\phi(t) = a_1 t + a_2 t^2$; 'The Second', which is determined by three parameters: the carrier frequency ($a_1$), the linear chirp ($a_2$), and the second order chirp ($a_3$), then the phase reads $\phi(t) = a_1 t + a_2 t^2 + a_3 t^3$; and 'The Roof', which is comprised of two parts, before central time and after, and is determined by three parameters: the carrier frequency ($a_1$), the linear chirp ($\tilde{a}_2$) for the first half of the pulse and the linear chirp ($\widetilde{\tilde{a}}_2$) for the second half of the pulse, then the constructed phase of the field reads $\phi(t) = a_1 t + \tilde{a}_2 t^2$ for $t \leq 0$, and $\phi(t) = a_1 t + \widetilde{\tilde{a}}_2 t^2$ for $t > 0$.

We simulated the pulses with these three kinds of phases using characteristic values of the field parameters and generated training data in quantity of $5 \times 10^4$ for each kind by varying the carrier frequency and the chirp rate. During the training process, we applied the Adam Optimizer algorithm with the learning rate of 0.1, and the regularization of 0.02 [54]. The loss function of the classification model is the cross entropy, but the mean squared error for the regression model. The early stop technique was also used to control the overfitting [55]. The details of the construction of the neural networks for both the classification and the regression models are presented in Appendix B.

After training the classification and the regression models, they are combined to be used as directed. The classification block classifies the random pulse and sends it to the corresponding regression block to solve for the analytical parameters of one of three kinds of the phase. The classification reaches the accuracy of 97.93%, and the overall root mean square error of the regression is smaller than 0.1, providing the deep learning model's results accurate enough. Both the classification and regression models are evaluated via a separate test data set, which contains $3 \times 10^3$ samples. To demonstrate high accuracy of the analytical fit to the numerical data of the phase of the field we show several prototypical phases in Fig.(4).

## IV. NUMERICAL RESULTS

Numerical analyses of the effects of the pulse shaping on the optimization of quantum coherence and mitigation of decoherence in the target molecules as well as the impact of multiple scattering from the target molecules are performed using the methanol molecule and addressing the Raman active symmetric mode having frequency 2837 $cm^{-1}$ (85.05 THz) [5]. This mode is chosen as a frequency unit [$\omega_{21}$]. The control scheme provides the selectivity of excitation of Raman active modes with the resolution up to $1/\tau$, where $\tau$ is a chirped pulse duration, which is about 2 to 3 $cm^{-1}$. Thus, the asymmetric stretch mode having frequency 2942 $cm^{-1}$ (88.20 THz) is not excited by the control scheme. The selectivity of excitation is not preserved when a broadband but transform-limited pulse trains are applied.

First we present the results of investigation of the dependence of the population and coherence on the peak Rabi frequency of the control pulses and reveal adiabatic type of solution leading to the maximum vibrational coherence. Then we analyze the four-level system dynamics subject to the interaction with the control pulse trains in the presence of decoherence and demonstrate a sustainable value of vibrational coherence. Finally, we show the solution of the Maxwell - Liouville von Neumann equations for the control pulse trains interacting with an ensemble of methanol molecules illustrating growth of the vibrational coherence and the anti-Stokes component of the propagating fields. Where appropriate, we compare the results with those for the transform-limited pulse trains interaction with the symmetric stretch mode in the CARS configuration.

### A. The analysis of the state population and coherence induced by the control pulses

Fig.(5(a)-(d)) shows the dependence of the populations and coherence as a function of the peak Rabi frequency for the case of the transform-limited pump, Stokes and probe pulses with zero and non-zero one-photon detuning (a),(c), and control pulses with zero and non-zero one-photon detuning (b),(d) respectively. The envelope of the Rabi frequency is the same for all three transform-limited pulses, which are also used as an initial condition for chirping in the control scheme. The values of the Rabi frequency on the abscissa are presented for the transform-limited pulse. Decoherence is not taken into account to get a clear

picture of the dependence of the state population and coherence on the Rabi frequencies. Under the one-photon resonance condition shown for the transform-limited pulses in (a) and for the chirped pulses in (b), the population of the excited states is significant, which prevents from achieving an equal population between the ground state $|1\rangle$ and the excited state $|2\rangle$. In the transform-limited pulse scenario in (a), coherence periodically becomes zero, which is not the case for the control pulses solution shown in (b). Such a behavior in (a) is due to the pulse area type of solution, when the probability amplitude of the states depends on the pulse area with $\pi$ value leading to the population inversion and $2\pi$ - to the population return. In contrast, the control pulse scheme provides adiabatic type of response in the four-level system with nonzero value of coherence, which depends on the strength of the fields as shown in (b). The one-photon detuning $\Delta_s = \Delta_{as} = \Delta = 1.0[\omega_{21}]$ minimizes the transitional population of the excited states $|3\rangle$ and $|4\rangle$ for both transform-limited and the control pulse scenario shown in (c) and (d) respectively. The one-photon detuning shifts the point of first zero coherence toward higher values of the Rabi frequencies in the transform-limited case in (c). In the control case in (d), the first point of equal population giving the maximum vibrational coherence occurs at the peak Rabi frequency $\Omega_{p0} = 0.75[\omega_{21}]$ and is achieved due to two-photon adiabatic passage with a negligible involvement of the excited state manifold into population dynamics. Beyond this point, coherence value varies within the range from 0.5 to 0.35 for the peak Rabi frequency $\Omega_{p0} = 1[\omega_{21}]$ and higher. Once coherence is built, it never drops to zero, in contrast to the transform-limited pulses solution. Thus, the detuned chirped pulse control scheme is more robust for the applications in CARS microscopy and spectroscopy because it provides one with a sustainable value of coherence resilient to fluctuations in the intensity of the Raman fields. To demonstrate adiabatic passage generated under the condition of nonzero one-photon detuning, a time-dependent picture is presented in Fig.(6(a-d)). The time dependence of the population and coherence in the four level system interacting with the transform-limited pump, Stokes and probe pulses, (a),(c), and with the control pulses, (b),(d) shows population dynamics and coherence for two values of the peak Rabi frequency $\Omega_p = 1.08$ and $1.5[\omega_{21}]$. The value of the Rabi frequency $\Omega_{p0} = 1.08[\omega_{21}]$ is chosen according to the Fig.(5(d)), which generates the second equal population between the ground state $|1\rangle$ and the excited state $|2\rangle$ and the maximum coherence $\rho_{21}$ in the control pulses scenario. It leads to adiabatic population transfer from the ground state $|1\rangle$ to the excited state $|2\rangle$. Meanwhile, the value of the peak

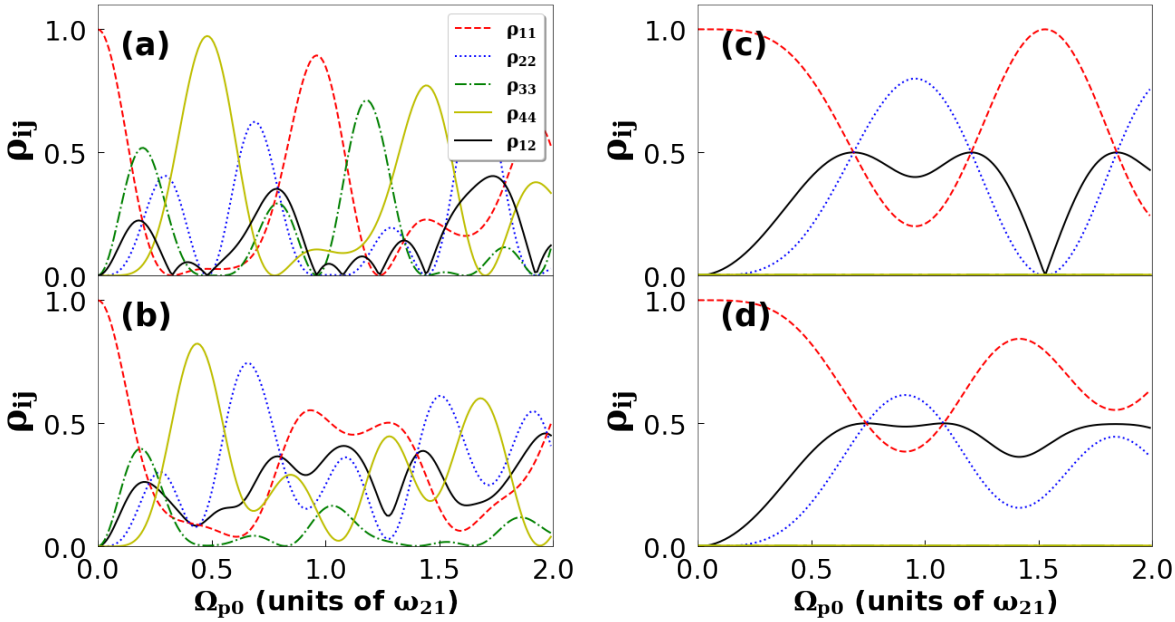


FIG. 5: The population and coherence in the four-level system as a function of the peak Rabi frequency $\Omega_p[\omega_{21}]$, which is the same for the pump, Stokes and probe pulses, $\omega_{21} = 85$ THz. Parameters used in the calculations are $\tau_0 = 4.66[\omega_{21}^{-1}], \Gamma = \gamma = 0$. In (a) the transform-limited pump, Stokes and probe pulses with zero one-photon detuning are applied, $\Delta_s = \Delta_{as} = \Delta = 0$; (b) the control pump, Stokes and probe pulses with zero one-photon detuning are applied $\alpha_s'/\tau_0^2 = -1.0, \Delta = 0$; (c) the transform-limited pulses with non-zero one-photon detuning are applied, $\Delta = 1.0[\omega_{21}]$; (d) Control pulses with non-zero one-photon detuning are applied, $\alpha_s'/\tau_0^2 = -1.0, \Delta = 1.0[\omega_{21}]$. Once coherence is built by the control pulses, it never drops to zero, in contrast to the transform-limited pulses solution. The detuned control scenario is robust for the applications in CARS microscopy and spectroscopy because it provides sustainable value of coherence resilient to fluctuations in the intensity of the Raman fields.

Rabi frequency $\Omega_{p0} = 1.5[\omega_{21}]$ is chosen because it gives the first zero coherence for the transform-limited pulse scenario in Fig.(5(c)), which is not the case for the control scheme in Fig.(5(d)). Parameter $\gamma$ is non-zero in order to see how spontaneous decay impacts state dynamics for the chosen representative values of the Rabi frequency. The time dependence of the populations and a significant coherence is still observed in (d) demonstrating benefits of the control scheme.

### B. The analysis of the four-level system dynamics subject to the interaction with the control pulse trains in the presence of decoherence

We analyze the impact of decoherence in the four-level system through its interaction with the control pump, Stokes and probe pulse trains each consisting of ten pulses in Fig.(7). The results in (a-d) are given for the peak Rabi frequency $\Omega_{p0} = 1.08[\omega_{21}]$, and the results in (e-h) for $\Omega_{p0} = 1.5[\omega_{21}]$. The value $\Omega_{p0} = 1.08[\omega_{21}]$ provides the maximum coherence (1/2) for the control pulse and high value of coherence (0.45) for the transform-limited pulse according to Fig.(5c,d), and the $\Omega_{p0} = 1.5[\omega_{21}]$ gives a contrast value of coherence for the control and the transform-limited pulse application, 0.39 and 0.07 respectively. We analyze the controllability and sustenance of vibrational coherence in the four-level system subject to a fast spontaneous decay and collisions ($\sim 10fs$); then we investigate the impact of vibrational relaxation considering the decay on the order of $1ps$ and demonstrate how the loss of coherence due to this process may be mitigated by periodically restoring population of the excited vibrational state $|2\rangle$ of the ground electronic state; and then we compare this result to the case when collisional dephasing is on the same order of magnitude ($\sim 1ps$).

Fast spontaneous decay and collisional dephasing rates ($10^{14}Hz$) of the transitional excited states $|3\rangle$ and $|4\rangle$ impact population dynamics and coherence even though these states are negligibly populated, shown in Fig.(7(a),(e)). Here populations and coherence $\rho_{21}$ are presented as a function of time for $\gamma_{4i} = \gamma_{3i} = \Gamma_{4i} = \Gamma_{3i} = 10^{14}Hz$, i=1,2. Population of states $|1\rangle \approx 0.6$ and $|2\rangle \approx 0.4$ is stable between pulses, but, even though $|3\rangle$ and $|4\rangle$ states are negligibly populated owing to the control scheme applied, their fast decoherence while pulse is on (chirped pulse duration is $55fs$) impacts populations of states $|2\rangle$ and $|1\rangle$ and coherence $\rho_{21}$ periodically drops to $\sim 0.02$. Between pulses, such a fast relaxation from the excited states leads to a reduced but stable value of coherence $\rho_{21} \sim 0.2$.

Fig.(7(b),(f)) shows the system dynamics in the presence of the vibrational relaxation of state $|2\rangle$ described by $\gamma_{21} = 10^{12}Hz$. Spontaneous decay from the excited states is also present, $\gamma_{4i} = \gamma_{3i} = \gamma_{21} = 10^{12}Hz; \Gamma_{4i} = \Gamma_{3i} = \Gamma_{21} = 0$. Figure demonstrates that coherence $\rho_{21}$ is periodically built up by the chirped pulses, and then insignificantly reduces its value between the pulses in the trains. Spontaneous decay rate $\gamma = 1THz$ from the excited state $|4\rangle$ to $|3\rangle$ does not make any contribution to the population dynamics and was neglected. However, because the pulse train period is chosen to match the decay time

$T = 1/\gamma_{21} = 1ps$, (and no collisional dephasing, $\Gamma_{ij} = 0$), the population of state $|2\rangle$ decreased due to spontaneous decay is periodically restored by control fields providing a sustainable value of coherence. When vibrational relaxation is much faster (e.g., $10^{14}Hz$) than the pulse repetition rate ($10^{12}Hz$), coherence $\rho_{21}$ becomes negligibly small between pulses (not shown here). Switching on collisional dephasing such that $\Gamma_{21} = \gamma_{21} = 1THz$ results in a more dramatical reduction of coherence $\rho_{21}$ as it is shown in Fig.(7(c),(g)) because collisional dephasing cannot be mitigated by this mechanism being represented by off-diagonal density matrix elements. However, the resultant coherence $\rho_{21}$ does not drop to zero between pulses. This is due to the choice of the pulse repetition rate as well as the control scheme leading to a negligible population of the excited states $|3\rangle$ and $|4\rangle$ in the dynamics. In contrast, the simultaneous application of the transform-limited pump, Stokes and probe pulse trains shown in Fig.(7(d),(h)) results in strong dependence of coherence on the peak Rabi frequency in accordance with the pulse area solution. The simultaneous application of the transform-limited pulses in this calculation aims to compare with the chirped pulses scenario. (Note, that within a different control scheme, e.g., F-STIRAP [56], which imposes a time delay between the Stokes and the pump pulses, the transform-limited pulses generate the maximum coherence.) The results of calculations presented in Fig.(7) for various values of the Rabi frequency of the control pulses and the transform-limited pulses led to a conclusion that for the control scheme there is vibrational coherence in the system for any value of the peak Rabi frequency within the adiabatic range, while for the related transform-limited pulse scenario this is not the case.

### C. The impact of Beer's law on the average intensity of propagating anti-Stokes signal

We apply Beer's law under the ideal conditions to evaluate the change in the amplitude of the anti-Stokes signal as pulses propagate through the atmosphere. I apply ten transform-limited pulses in the pulse train. Numerical analysis shows that the amplitude of the pump, Stokes and probe pulse trains is reduced upon propagation, while the average intensity of the anti-Stokes pulse trains is amplified as shown in Fig.(8) for propagation through 699 layers for both cases, with and without impact from the air. The intensity of the anti-Stokes pulse trains in the presence of the air is depreciated due to the scattering and absorption

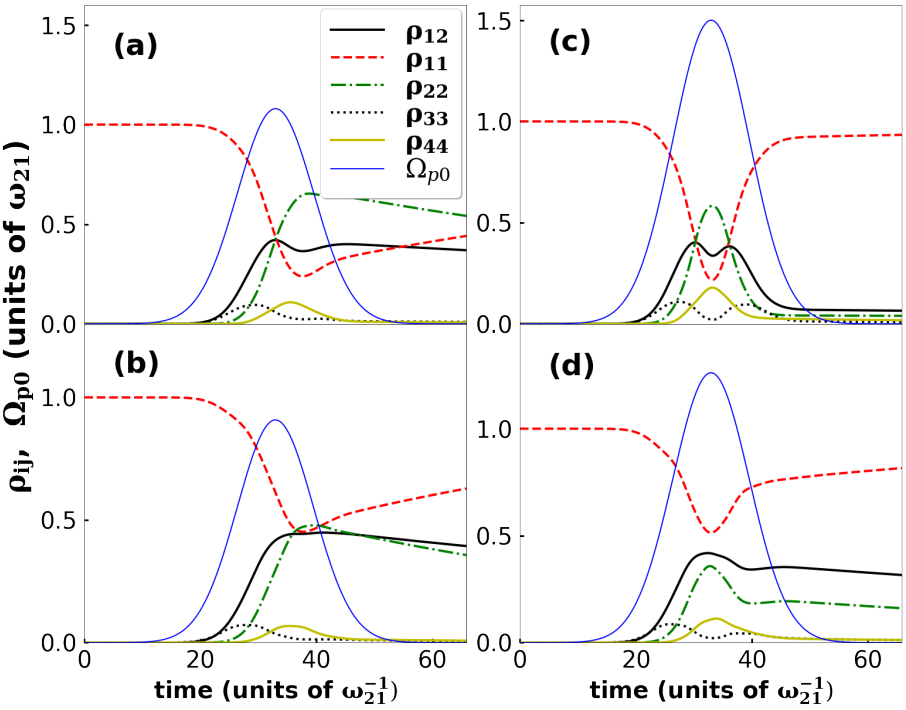


FIG. 6: Dynamics of the population of four states $\rho_{11}$ (dashed red), $\rho_{22}$ (dash-dotted green), $\rho_{33}$ (dotted black), $\rho_{44}$ (solid yellow) and coherence $\rho_{21}$ (solid black) in the four-level system interacting with the transform-limited pump, Stokes and probe pulses in (a),(c); and the control pulses in (b),(d), $\alpha_s'/\tau_0^2 = -1.0$ for the peak Rabi frequency of the pump, the Stokes and the probe pulses, (before chirping for the control scheme), $\Omega_p = 1.08$ $[\omega_{21}]$ in (a),(b), and 1.5 $[\omega_{21}]$ in (c),(d). Other parameters are $\tau_0 = 4.66$ $[\omega_{21}^{-1}]$, all $\gamma_{ij} = \gamma = 1.176 \times 10^{-2}[\omega_{21}], \Gamma = 0, \Delta = 1.0[\omega_{21}]$.

effects.

### D. The analysis of the Maxwell - Liouville von Neumann equations and demonstration of a generation of the anti-Stokes signal

Using Maxwell's equations Eqs.(8) coupled to the Liouville von Neumann equations Eqs. (9) we numerically analyzed the propagation effects of the control pump, Stokes, probe and the generated anti-Stokes fields scattered from the target molecules and observed the amplification of the anti-Stokes component. The machine learning approach was implemented to reveal the modulation of the phase of four field components after each scattering Fig.(9) shows the control pump, Stokes, probe and the built-up anti-Stokes pulses after each of five consecutive scattering events for the parameters of the fields $\Omega_{p(s,pr)} = 85THz$

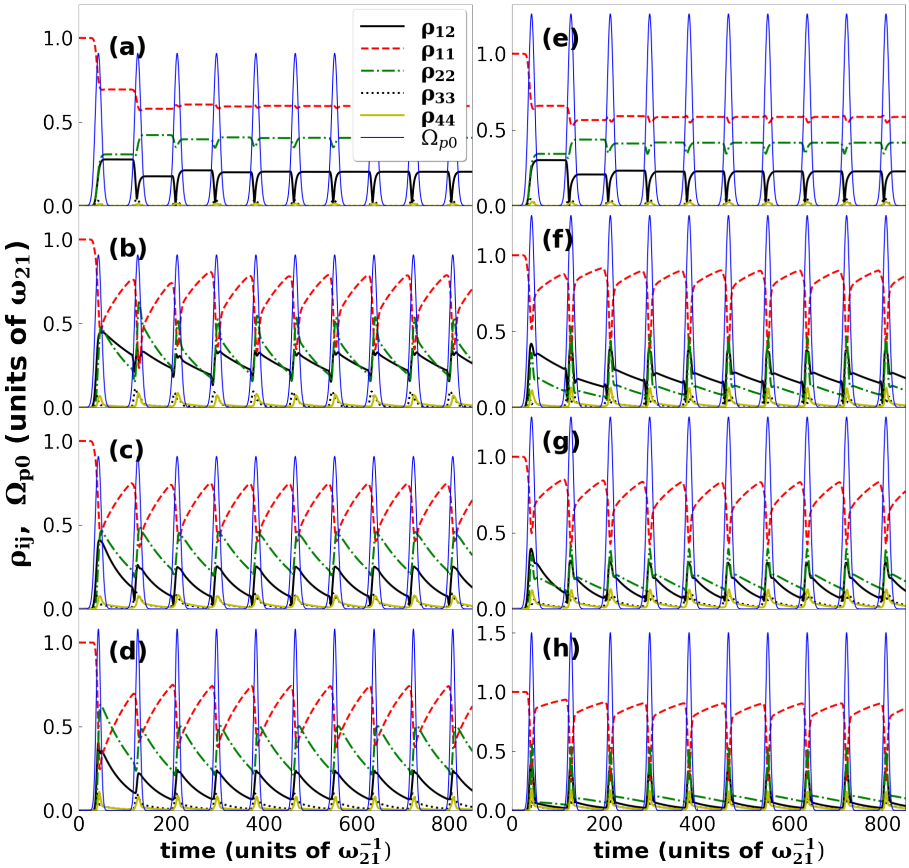


FIG. 7: Dynamics of the population of four states $\rho_{11}$ (dashed red), $\rho_{22}$ (dash-dotted green), $\rho_{33}$ (dotted black), $\rho_{44}$ (solid yellow) and coherence $\rho_{21}$ (solid black) in the four-level system interacting with the control pulse trains having the repetition rate of 1 THz and the value of the peak Rabi frequency in (a-d) equal to $\Omega_{p0} = 1.08[\omega_{21}]$, and in (e-h) equal to $\Omega_{p0} = 1.5[\omega_{21}]$. In (a),(e) $\gamma_{4i} = \gamma_{3i} = \Gamma_{4i} = \Gamma_{3i} = 10^{14}Hz$, i=1,2, but no vibrational relaxation, $\gamma_{21} = \Gamma_{21} = 0$; in (b),(f) $\gamma_{4i} = \gamma_{3i} = \gamma_{21} = 10^{12}Hz; \Gamma_{4i} = \Gamma_{3i} = \Gamma_{21} = 0$; in (c),(g) $\gamma_{4i} = \gamma_{3i} = \Gamma_{4i} = \Gamma_{3i} = \gamma_{21} = \Gamma_{21} = 10^{12}Hz$; and (d),(h) the four-level system interacting with the transform-limited pulse trains and $\gamma_{4i} = \gamma_{3i} = \Gamma_{4i} = \Gamma_{3i} = \gamma_{21} = \Gamma_{21} = 10^{12}Hz$. The rest field parameters are $\tau_0 = 4.66[\omega_{21}^{-1}], \Delta_s = \Delta_{as} = 1.0[\omega_{21}]$ and $\alpha_s'/\tau_0^2 = -1.0$ for the control pulse scenario.

$(E_{p(s,pr)_0} \sim 1.6 \times 10^9 V/m)$, $\tau_0 = 54.8fs$, $\alpha_s = -7THz/fs$, and $\Delta_s = \Delta_{as} = \Delta = 850THz$. The neural networks explained in the previous section were optimized to work for these parameters. The classifier neural network predicted the pulses as the third kind described above and the regression neural network provided the chirping parameters. After 5 scatter-

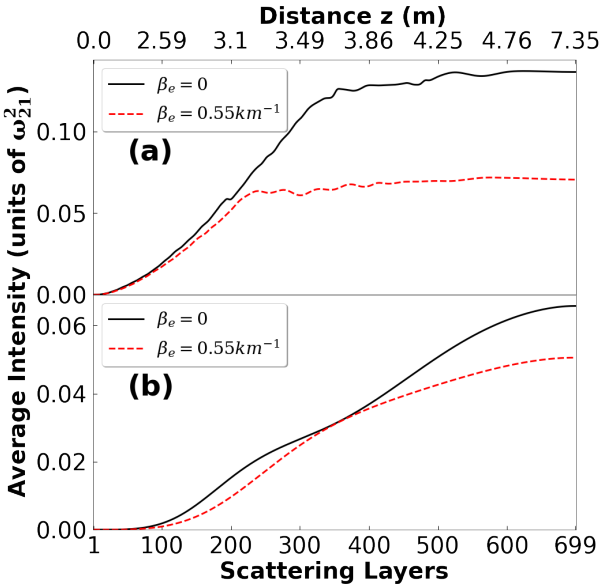


FIG. 8: An average intensity of the anti-Stokes pulses as a function of the number of scattering layers calculated applying Beer's law to the propagation of a transform-limited pulse train consisting of 10 pulses. The black solid curve represents the change in the average intensity as pulses undergo scattering through layers for the case of $\beta_e = 0$ (without taking air into consideration), and red dashed curves shows for $\beta_e = 0.55\ km^{-1}$. The one-photon detuning is $\Delta = 1[\omega_{21}]$ in (a), and $\Delta = 10[\omega_{21}]$ in (b). The width of the target molecules distribution is $\sigma = 1m$. The depreciation of intensity is due to scattering and absorption in the air.

ing events, the change in the initial chirp rate $\alpha_s$ is less than 0.001% indicating that the control scheme would work for large number of layers. The anti-Stokes component is built up having the peak Rabi frequency about $10^{-6}\Omega_p$ after the fifth iteration.

We also analyzed propagation effects using the transform-limited pump, Stokes, and probe pulse trains having the peak Rabi frequency $\Omega_{p(s,pr)} = 85THz = \omega_{21}$ and been largely detuned from the one-photon transitions, the detuning is $\Delta_s = \Delta_{as} = \Delta = 10\omega_{21} = 850THz$ for the adiabatic regime. We consider 10 pulses in the pulse train having period $T = 1ps$. The increase of the peak value of the anti-Stokes Rabi frequency $\Omega_{as}(t)$ by two orders of magnitude is observed 1 meter (199 layers) away from the peak molecular density. Coherence is increasing from pulse to pulse and the population is adiabatically transferred from the ground state $|1\rangle$ to the excited state $|2\rangle$ in the four-level system during the interaction with four fields in the CARS configuration. Here adiabatic regime is achieved due to a large

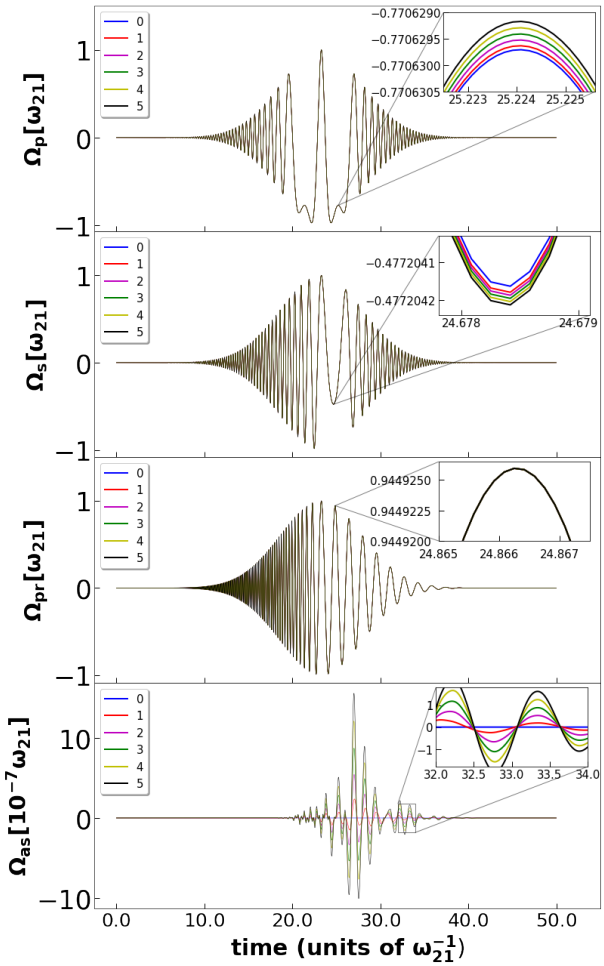


FIG. 9: The pump, the Stokes, the probe and the built-up anti-Stokes chirped pulses after each of five consecutive scattering events. 0,1,2,3,4,5 represent incoming, 1st, 2nd, 3rd, 4th and 5th scattering event respectively. The incident pulses are chirped in accordance with the control scheme. The parameters of the fields are $\Omega_{p(s,pr)} = 85THz$ ($E_{p(s,pr)_0} \sim 1.6 \times 10^9 V/m$), $\tau_0 = 54.8fs$, $\alpha_s = -7THz/fs$, and $\Delta_s = \Delta_{as} = \Delta = 850THz$. The anti-Stokes field is built up gradually and constitutes $\sim 10^{-6}$ of the amplitude of the incident field.

one-photon detuning $\Delta = 10\omega_{21}$ and the choice of the peak Rabi frequency $\Omega_{p(s,pr)} = \omega_{21}$, which result in a negligible population of the transitional states $|3\rangle$ and $|4\rangle$.

From the results above it follows that the implementation of the control pulse trains in the four-wave mixing in CARS is more robust for the generation of a sustainable anti-Stokes backscattered signal compared to the use of a set of transform-limited pulses. This is due to the adiabatic regime of light-matter interaction which preserves vibrational coherence and facilitates a built-up of the anti-Stokes signal. For the case of the phase-matching

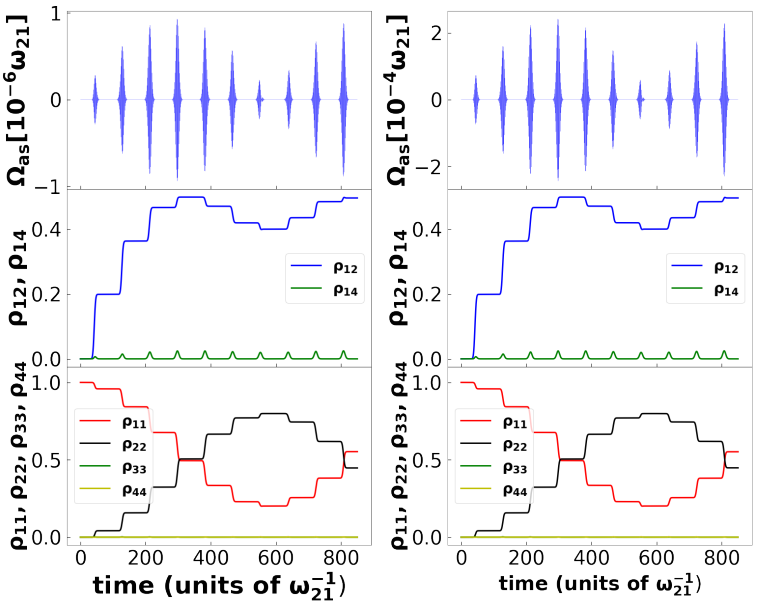


FIG. 10: Scattering dynamics using the transform-limited pump, Stokes, and probe pulse trains having the peak Rabi frequency equal to the frequency between states $|1\rangle$ and $|2\rangle$, $\Omega_{p(s,pr)_0} = \omega_{21}$, and been largely detuned from the one-photon transitions, the detuning is $\Delta_s = \Delta_{as} = \Delta = 10\omega_{21} = 850THz$ for adiabatic regime. There are 10 pulses in each pulse train. The first raw shows ten anti-Stokes pulses (top), the state coherence (middle) and populations (bottom) after the first scattering event; the second raw shows the same after the 199th scattering event. Parameters $\sigma = 0.2m$; 199 layers provide a distance of 1 m away from the peak molecular density; $\tau_0 = 54.8fs$; $T = 1ps$.

conditions relaxed, given the size of the molecules is less than the wavelength of the incident fields, a collinear copropagating configuration of CARS may be created using the methanol as a surrogate target. Because the anti-Stokes radiation is generated as a result of the stimulated Raman scattering process, it is highly directional and is built up in the forward and the backward directions dominantly [22, 57]. Therefore, the backscattered anti-Stokes signal will reach a detector near the laser source. The following parameters of the fields may be used in an experiment: the pulse duration of order $100fs$, the peak field amplitude of $E_{0p(s,pr)} \sim 1.6 \times 10^9 V/m$; the control pulse chirps obeying the relationship $\alpha_s = -\alpha_p$, and $\alpha_{pr} = \alpha_s - \alpha_p$ for the first half of the pulse duration $t \leq t_c$, and $\alpha_s = \alpha_p$, $\alpha_{pr} = 0$ for $t > t_c$; the value of $\alpha_s = -7THz/fs$, the pulse train period of order of spontaneous decay time and the one-photon detuning of order $\Delta \sim 1/fs$.

## V. SUMMARY

We present a semiclassical theory of the four-wave mixing process in the coherent anti-Stokes Raman scattering implementing the control pulse trains. The theory is based on a set of Maxwell's equations for propagation of the pump, the Stokes, the probe and the anti-Stokes components of the fields coupled to the Liouville von Neumann equations with relaxation for dynamics in the target molecules. It is intended for the investigations of the remote detection of biochemical molecules. The multi-layer model is developed to account for the spatial distribution of the target molecules in the air mimicking the environmental conditions. The machine learning approach is developed to analyze the evolving phase of the pulse trains as they undergo scattering within each layer. The approach makes use of the deep Convolutional Neural Network. The quantum control method for the incident pulse shaping is implemented, which optimizes the macroscopic induced polarization in the target molecules by maximizing vibrational coherence. The method implies chirping of the incident pulse trains, which induce adiabatic population transfer within four states in the CARS scheme leading to a sustainable, high vibrational coherence. Importantly, the transitional excited states get negligibly populated, thus minimizing the impact of spontaneous decay and associated losses of coherence from these states. Moreover, the choice of the pulse train period to match the spontaneous decay time permits for mitigation of the vibrational decay. The enhancement of the anti-Stokes field is observed upon propagation through the ensemble of the target molecules, achieved by the control pulse trains as well as by the transform-limited pulse trains with a large detuning and a carefully chosen Rabi frequency. The coherent enhancement of the anti-Stokes signal and mitigation of decoherence by chirped control fields form a foundation for the propagation of the anti-Stokes signal through distances on a kilometer scale.

## VI. ACKNOWLEDGEMENT

The authors gratefully acknowledge support from the Office of Naval Research.

### Appendix A: Derivation of Maxwell - Liouville von Neumann Equations

Maxwell's equations, with no free currents and charges, read

$$\nabla \cdot (\epsilon_0 E + P) = 0 \tag{A1}$$

$$\nabla \times E = -\partial B/\partial t \tag{A2}$$

$$\nabla \times B = \mu_0 \partial(\epsilon_0 + P)/\partial t \tag{A3}$$

$$\nabla \cdot B = 0 \tag{A4}$$

From Eqs.(A2,A3) we obtain the wave equation

$$\nabla^2 E - \epsilon_0 \mu_0 \frac{\partial^2 E}{\partial^2 t} = \nabla(\nabla \cdot E) + \mu_0 \frac{\partial^2 P}{\partial^2 t}. \tag{A5}$$

It follows from Eq.(A1) that $\nabla \cdot E = \nabla \cdot P/\epsilon_0$ in a space free from charges. In a plane wave limit, when the wave length is much less than the beam radius and neglecting any diffraction effects in transverse direction, fields propagate in the $\hat{z}$ direction and have polarization in the XY plane. Then $\nabla \cdot P$ may be set to zero and the wave equation reads

$$\left(\frac{\partial}{\partial z} + \frac{1}{c}\frac{\partial}{\partial t}\right)\left(-\frac{\partial}{\partial z} + \frac{1}{c}\frac{\partial}{\partial t}\right) E = -\mu_0 \frac{\partial^2 P}{\partial t^2} \tag{A6}$$

Assuming the field is $E(z,t) = \frac{1}{2}(E_0(z,t)e^{-i[\omega t - kz - \phi(z,t)]} + c.c)$ and polarization is $P(z,t) = \frac{1}{2}(P_0(z,t)e^{-i[\omega t - kz - \phi(z,t)]} + c.c)$ and considering $E_0(z,t)$ and $\phi(z,t)$ as slowly varying functions of position and time, we write

$$\begin{aligned} -\frac{\partial E(z,t)}{\partial z} = -\frac{1}{2}(&e^{-i\omega t}e^{ikz}e^{i\phi(z,t)}\frac{\partial E_0(z,t)}{\partial z} + ikE_0(z,t)e^{-i\omega t}e^{ikz}e^{i\phi(z,t)} \\ &+ i\frac{\partial \phi(z,t)}{\partial z}E_0(z,t)e^{-i\omega t}e^{ikz}e^{i\phi(z,t)} + c.c.) \end{aligned} \tag{A7}$$

$$\begin{aligned} \frac{1}{c}\frac{\partial E(z,t)}{\partial t} = \frac{1}{2c}(&e^{-i\omega t}e^{ikz}e^{i\phi(z,t)}\frac{\partial E_0(z,t)}{\partial t} - i\omega E_0(z,t)e^{-i\omega t}e^{ikz}e^{i\phi(z,t)} \\ &+ i\frac{\partial \phi(z,t)}{\partial t}E_0(z,t)e^{-i\omega t}e^{ikz}e^{i\phi(z,t)} + c.c.) \end{aligned} \tag{A8}$$

Then

$$\begin{aligned} \left(-\frac{\partial}{\partial z} + \frac{1}{c}\frac{\partial}{\partial t}\right) E &= -\frac{ik}{2}(E_0(z,t)e^{-i\omega t}e^{ikz}e^{i\phi(z,t)} - c.c.) \\ &\quad -\frac{i\omega}{2c}(E_0(z,t)e^{-i\omega t}e^{ikz}e^{i\phi(z,t)} - c.c.) \\ &= -ik(E_0(z,t)e^{-i(\omega t - kz - \phi(z,t))} - c.c.) = -2ik\,\mathrm{Im}\{E\}. \end{aligned} \tag{A9}$$

By substituting Eq.(A9) to Eq.(A6) and using $\omega/c = k$ and later assuming real fields we arrive at

$$\begin{aligned}
-ik\left(\tfrac{\partial}{\partial z}+\tfrac{1}{c}\tfrac{\partial}{\partial t}\right)\left(E_0(z,t)e^{-i(\omega t-kz-\phi(z,t))}+c.c.\right) = \\
-ik\tfrac{\partial E_0(z,t)}{\partial z}e^{-i(\omega t-kz-\phi(z,t))}+ik\tfrac{\partial E_0^*(z,t)}{\partial z}e^{i(\omega t-kz-\phi(z,t))} \\
-\tfrac{ik}{c}\tfrac{\partial E_0(z,t)}{\partial t}e^{-i(\omega t-kz-\phi(z,t))}+\tfrac{ik}{c}\tfrac{\partial E_0^*(z,t)}{\partial t}e^{i(\omega t-kz-\phi(z,t))} = \\
-ik\left[\left(\tfrac{\partial E_0(z,t)}{\partial z}+\tfrac{1}{c}\tfrac{\partial E_0(z,t)}{\partial t}\right)e^{-i(\omega t-kz-\phi(z,t))}-\left(\tfrac{\partial E_0^*(z,t)}{\partial z}+\tfrac{1}{c}\tfrac{\partial E_0^*(z,t)}{\partial t}\right)e^{i(\omega t-kz-\phi(z,t))}\right] = \\
-2k\left(\tfrac{\partial E_0(z,t)}{\partial z}+\tfrac{1}{c}\tfrac{\partial E_0(z,t)}{\partial t}\right)\tfrac{1}{2i}\left(-e^{-i(\omega t-kz-\phi(z,t))}+e^{i(\omega t-kz-\phi(z,t))}\right) \\
= -2k\left(\tfrac{\partial E_0(z,t)}{\partial z}+\tfrac{1}{c}\tfrac{\partial E_0(z,t)}{\partial t}\right)\sin\left(\omega t-kz-\phi(z,t)\right) = \\
-\mu_0\tfrac{\partial^2}{\partial t^2}P(z,t)
\end{aligned} \tag{A10}$$

For $P(z,t) = \frac{1}{2}(P_0(z,t)e^{-i[\omega t-kz-\phi(z,t)]}+c.c)$,

$$\frac{\partial^2}{\partial t^2}P(z,t) = -\omega^2\left(\frac{1}{2}(P_0(z,t)e^{-i[\omega t-kz-\phi(z,t)]}+c.c)\right) = -\omega^2\,\mathrm{Re}\left[P(z,t)\right] \tag{A11}$$

Substituting these in Eq.(A10) gives

$$\begin{aligned}
-2k(\tfrac{\partial E_0(z,t)}{\partial z}+\tfrac{1}{c}\tfrac{\partial E_0(z,t)}{\partial t})\sin\left(\omega t-kz-\phi(z,t)\right) = \\
\mu_0\omega^2\left(Re\left[P_0(z,t)\right]\cos\left(\omega t-kz\right)+Im\left[P_0(z,t)\right]\sin\left(\omega t-kz-\phi(z,t)\right)\right),
\end{aligned} \tag{A12}$$

leading to

$$-2k(\tfrac{\partial E_0(z,t)}{\partial z}+\tfrac{1}{c}\tfrac{\partial E_0(z,t)}{\partial t}) = \mu_0\omega^2 Im\left[P_0(z,t)\right]. \tag{A13}$$

In quantum theory, a measurable quantity is the expectation value, which for macroscopic polarization is an expectation value of the electric dipole moment operator $\hat{\mu}$, $\langle P(z,t)\rangle = N_s Tr\{\langle\rho(z,t)\cdot\mu\rangle\}$, where $N_s$ is the atomic density of the target molecules. Applied to the four-level system of CARS, it contains four components corresponding to each of four transitions:

$$\begin{aligned}
P_p(z,t) &= 2N_s\,\mathrm{Re}\left[\mu_{13}\rho_{13}(z,t)e^{i(\omega_p t-k_p z-\phi(z,t))}\right] \\
P_s(z,t) &= 2N_s\,\mathrm{Re}\left[\mu_{23}\rho_{23}(z,t)e^{i(\omega_s t-k_s z-\phi(z,t))}\right] \\
P_{pr}(z,t) &= 2N_s\,\mathrm{Re}\left[\mu_{24}\rho_{24}(z,t)e^{i(\omega_{pr} t-k_{pr} z-\phi(z,t))}\right] \\
P_{as}(z,t) &= 2N_s\,\mathrm{Re}\left[\mu_{14}\rho_{14}(z,t)e^{i(\omega_{as} t-k_{as} z-\phi(z,t))}\right],
\end{aligned} \tag{A14}$$

giving $P_{0p}(z,t) = N_s\mu_{13}\rho_{13}(z,t)$, $P_{0s}(z,t) = N_s\mu_{23}\rho_{23}(z,t)$, $P_{0pr}(z,t) = N_s\mu_{24}\rho_{24}(z,t)$, and $P_{0as}(z,t) = N_s\mu_{14}\rho_{14}(z,t)$.

For four components of propagating fields in CARS, the Eq.(A13) reads as follows

$$\begin{aligned}
\tfrac{\partial E_p}{\partial z} + \tfrac{1}{c}\tfrac{\partial E_p}{\partial t} &= -N_s\tfrac{\mu_0\mu_{13}\omega_p^2}{k_p}\,\mathrm{Im}\{\rho_{13}(z,t)\} \\
\tfrac{\partial E_s}{\partial z} + \tfrac{1}{c}\tfrac{\partial E_s}{\partial t} &= -N_s\tfrac{\mu_0\mu_{23}\omega_s^2}{k_s}\,\mathrm{Im}\{\rho_{23}(z,t)\} \\
\tfrac{\partial E_{pr}}{\partial z} + \tfrac{1}{c}\tfrac{\partial E_{pr}}{\partial t} &= -N_s\tfrac{\mu_0\mu_{24}\omega_{pr}^2}{k_{pr}}\,\mathrm{Im}\{\rho_{24}(z,t)\} \\
\tfrac{\partial E_{as}}{\partial z} + \tfrac{1}{c}\tfrac{\partial E_{as}}{\partial t} &= -N_s\tfrac{\mu_0\mu_{14}\omega_{as}^2}{k_{as}}\,\mathrm{Im}\{\rho_{14}(z,t)\}.
\end{aligned} \tag{A15}$$

If $\bar{t} = (t - \frac{z}{c})$, then $\frac{\mathrm{d}t}{\mathrm{d}z} = (\frac{\mathrm{d}\bar{t}}{\mathrm{d}z} + \frac{1}{c})$, which leads to $\frac{\partial}{\partial z} = \frac{\partial}{\partial t}\frac{\partial t}{\partial z} = \frac{1}{c}\frac{\partial}{\partial t}$. Taking into account that $k_q = \omega_q/c$, and $c\omega_q\hbar = E_q$, where $q = p, s, pr, as$, the Eq. (A15) becomes

$$\frac{1}{c}\frac{\partial E_q}{\partial t} = -N_s\mu_0\mu_{ij}\frac{E_q(t)}{\hbar}\,\mathrm{Im}\{\rho_{ij}\} \tag{A16}$$

We find the density matrix elements $\rho_{ij}$ from the Liouville von Neumann equation $i\hbar\dot{\rho} = [H, \rho]$ and using the above Hamiltonian in Eq.(2). We start by opening the commutator and applying the substitutions

$$\begin{aligned}
\rho_{12} &= \tilde{\rho}_{12}e^{i(\alpha_p-\alpha_s)t^2/2} \\
\rho_{13} &= \tilde{\rho}_{13}e^{i(\Delta_s t+\alpha_p t^2/2)} \\
\rho_{14} &= \tilde{\rho}_{14}e^{i\Delta_{as}t} \\
\rho_{23} &= \tilde{\rho}_{23}e^{i(\Delta_s t+\alpha_s t^2/2)} \\
\rho_{24} &= \tilde{\rho}_{24}e^{i(\Delta_{as}t+\alpha_{pr}t^2/2)} \\
\rho_{34} &= \tilde{\rho}_{34}e^{i(\Delta_{as}-\Delta_s)t-i\alpha_p t^2/2}
\end{aligned} \tag{A17}$$

Next, we apply the rotating wave approximation and use the control condition on the chirp

parameters $\alpha_s - \alpha_p = \alpha_{pr}$, and arrive at

$$
\begin{aligned}
\dot{\rho}_{11} &= -i\Omega_{p0}(t)/2\tilde{\rho}_{31} + i\Omega^*_{p0}(t)/2\tilde{\rho}_{13} - i\Omega_{as0}(t)/2\tilde{\rho}_{41} + i\Omega^*_{as0}(t)/2\tilde{\rho}_{14} \\
\dot{\rho}_{22} &= -i\Omega_{s0}(t)/2\tilde{\rho}_{32} + i\Omega^*_{s0}(t)/2\tilde{\rho}_{23} - i\Omega_{pr0}(t)/2\tilde{\rho}_{42} + i\Omega^*_{pr0}(t)/2\tilde{\rho}_{24} \\
\dot{\rho}_{33} &= i\Omega_{p0}(t)/2\tilde{\rho}_{31} - i\Omega^*_{p0}(t)/2\tilde{\rho}_{13} + i\Omega_{s0}(t)/2\tilde{\rho}_{32} - i\Omega^*_{s0}(t)/2\tilde{\rho}_{23} \\
\dot{\rho}_{44} &= i\Omega_{as0}(t)/2\tilde{\rho}_{41} - i\Omega^*_{as0}(t)/2\tilde{\rho}_{14} + i\Omega_{pr0}(t)/2\tilde{\rho}_{42} - i\Omega^*_{pr0}(t)/2\tilde{\rho}_{24} \\
\dot{\tilde{\rho}}_{12} &= i\alpha_{pr}t\tilde{\rho}_{12} - i\Omega_{p0}(t)/2\tilde{\rho}_{32} - i\Omega_{as0}(t)/2\tilde{\rho}_{42} + i\Omega^*_{s0}(t)/2\tilde{\rho}_{13} + i\Omega^*_{pr0}(t)/2\tilde{\rho}_{14} \\
\dot{\tilde{\rho}}_{13} &= -i(\Delta_s + \alpha_p t)\tilde{\rho}_{13} - i\Omega_{p0}(t)/2(\rho_{33} - \rho_{11}) - i\Omega_{as0}(t)/2\tilde{\rho}_{43} + i\Omega_{s0}(t)/2\tilde{\rho}_{12} \\
\dot{\tilde{\rho}}_{14} &= -i\Delta_{as}\tilde{\rho}_{14} - i\Omega_{p0}(t)/2\tilde{\rho}_{34} - i\Omega_{as0}(t)/2(\rho_{44} - \rho_{11}) + i\Omega_{pr0}(t)/2\tilde{\rho}_{12} \\
\dot{\tilde{\rho}}_{23} &= -i(\Delta_s + \alpha_s t)\tilde{\rho}_{23} - i\Omega_{s0}(t)/2(\rho_{33} - \rho_{22}) - i\Omega_{pr0}(t)/2\tilde{\rho}_{43} + i\Omega_{p0}(t)/2\tilde{\rho}_{21} \\
\dot{\tilde{\rho}}_{24} &= -i(\Delta_{as} + \alpha_{pr} t)\tilde{\rho}_{24} - i\Omega_{pr0}(t)/2(\rho_{44} - \rho_{22}) - i\Omega_{s0}(t)/2\tilde{\rho}_{34} + i\Omega_{as0}(t)/2\tilde{\rho}_{21} \\
\dot{\tilde{\rho}}_{34} &= i(\Delta_s - \Delta_{as} + \alpha_p t)\tilde{\rho}_{34} - i\Omega^*_{p0}(t)/2\tilde{\rho}_{14} - i\Omega^*_{s0}(t)/2\tilde{\rho}_{24} + i\Omega_{as0}(t)/2\tilde{\rho}_{31} + i\Omega_{pr0}(t)/2\tilde{\rho}_{32}.
\end{aligned}
$$

After performing adiabatic elimination of the excited states assuming that $\dot{\rho}_{13}, \dot{\rho}_{14}, \dot{\rho}_{23}, \dot{\rho}_{24}, \dot{\rho}_{34} \approx 0$, $\rho_{34} \approx 0$, $\rho_{33}, \rho_{44} \ll \rho_{11}, \rho_{22}$ and $\dot{\rho}_{33}, \dot{\rho}_{44} \approx 0$, the density matrix elements $\rho_{13}, \rho_{23}, \rho_{14}, \rho_{24}$ read in terms of $\rho_{11}, \rho_{22}$ and $\rho_{12}$ as follows

$$
\begin{aligned}
\rho_{13} &= \frac{1}{2(\Delta_s + \alpha_p t)}\Omega_{p0}(t)\rho_{11} + \frac{1}{2(\Delta_s + \alpha_p t)}\Omega_{s0}(t)\rho_{12} \\
\rho_{23} &= \frac{1}{2(\Delta_s + \alpha_s t)}\Omega_{s0}(t)\rho_{22} + \frac{1}{2(\Delta_s + \alpha_s t)}\Omega_{p0}(t)\rho_{21} \\
\rho_{14} &= \frac{1}{2\Delta_{as}}\Omega_{as0}(t)\rho_{11} + \frac{1}{2\Delta_{as}}\Omega_{pr0}(t)\rho_{12} \\
\rho_{24} &= \frac{1}{2(\Delta_{as} + \alpha_{pr} t)}\Omega_{pr0}(t)\rho_{22} + \frac{1}{2(\Delta_{as} + \alpha_{pr} t)}\Omega_{as0}(t)\rho_{21}
\end{aligned}
\tag{A18}
$$

Substituting Eq.(A18) in Eq.(A16) and rewriting the equations in terms of Rabi frequencies provide the following Maxwell's equations:

$$
\begin{aligned}
\frac{\partial \Omega_{p0}}{\partial t} &= c\frac{\partial \Omega_{p0}}{\partial z} = -\frac{\eta}{2(\Delta_s + \alpha_p t)}\kappa_{13}\omega_p\Omega_{s0}(t)\,\mathrm{Im}[\rho_{12}] \\
\frac{\partial \Omega_{s0}}{\partial t} &= c\frac{\partial \Omega_{s0}}{\partial z} = \frac{\eta}{2(\Delta_s + \alpha_s t)}\kappa_{23}\omega_s\Omega_{p0}(t)\,\mathrm{Im}[\rho_{12}] \\
\frac{\partial \Omega_{pr0}}{\partial t} &= c\frac{\partial \Omega_{pr0}}{\partial z} = \frac{\eta}{2(\Delta_{as} + \alpha_{pr} t)}\kappa_{24}\omega_{pr}\Omega_{as0}(t)\,\mathrm{Im}[\rho_{12}] \\
\frac{\partial \Omega_{as0}}{\partial t} &= c\frac{\partial \Omega_{as0}}{\partial z} = -\frac{\eta}{2(\Delta_{as})}\kappa_{14}\omega_{as}\Omega_{pr0}(t)\,\mathrm{Im}[\rho_{12}].
\end{aligned}
\tag{A19}
$$

### Appendix B: The structure of the Deep Neural Networks

Both the classification and the regression neural networks share the same core structure. Since the numerical pulses, which we generated as the training data, have 2500 time steps, all models have the input shape of $2500 \times 1$. There are three blocks of the mini-convolutional neural network in the models. The first block contains three 1D convolutional layers with the kernel size of 3. The second block has two layers of the 1D convolutional network with kernel size of 5. The third block has a single 1D convolutional layer of kernel of 7. All the convolutional layers are activated by the Rectified Linear Units Function [58] and the Group Normalization [59]. There is a maximum pooling layer of pool size 4 after each block. There is a linear layer of size 1024 after the output of the convolutional blocks is flattened.

The structure of the neural network, shown in Fig.(11), is determined by the validation results, together with the other hyperparameters, such as the learning rate, the choice of optimizer and regularization. We adjust the kernel size, the number of blocks and the number of layers in each block to have the optimal validation result. The 1D convolution layers are used because they are suitable for extracting the information within the sub-region of the whole input tensor. It is a match to our aim, which is to extract the instantaneous value of the analytical parameter from the numerical sequential, time-dependent data. Besides, we use several 1D convolution layers as a block to extract the high dimension information from the input tensor. Three kernels of size of 3 cover the same area of the input tensor as a single kernel of size of 7, but the former catches the higher dimension information than the later one. We didn't set all blocks to three layers of kernel size of 3 because we would like to control the overfitting problem.

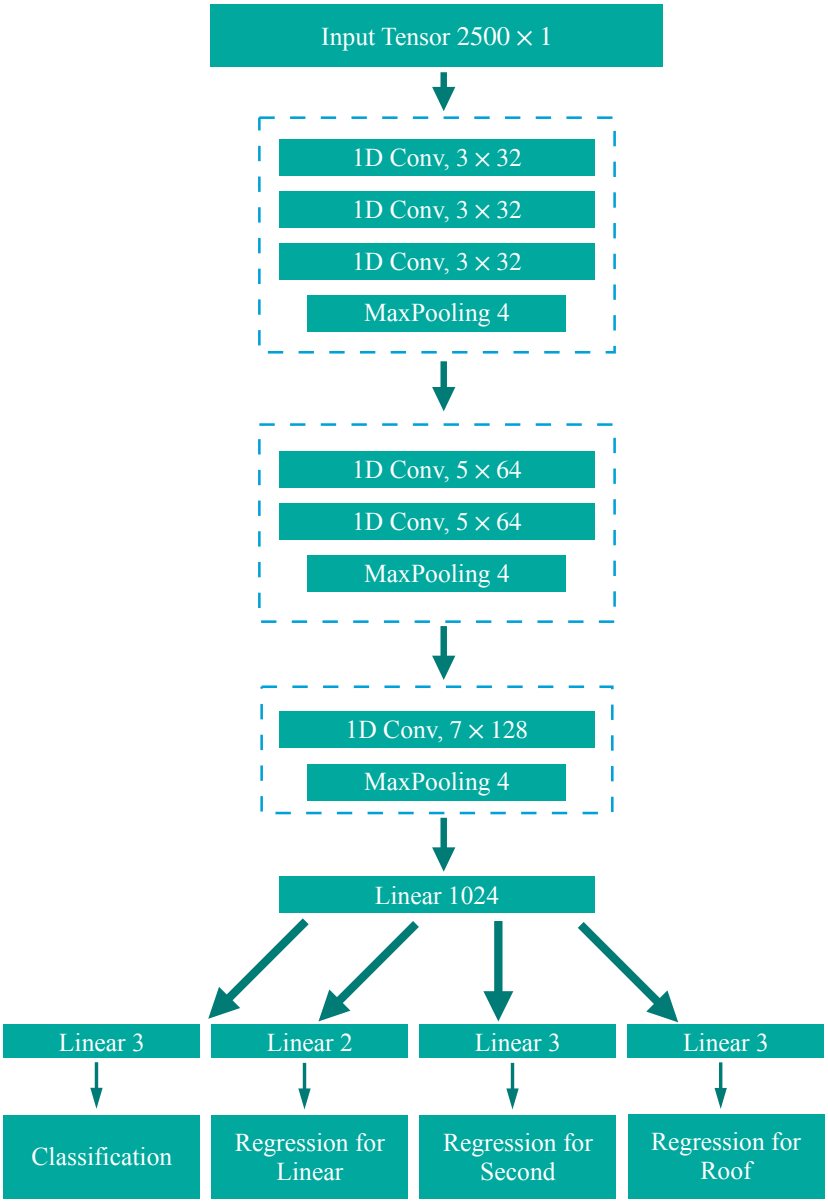


FIG. 11: The structure of the Deep Neural Network. The same structure is shared by the phase type classifier and the three phase value regression models, except for the last output layer. Three convolutional blocks are used sequentially to extract the highly non-linear information from the input time dependent tensor. The linear layer is used after flatten the output from the last convolutional block.

[1] *Coherent Raman Scattering Microscopy,* Eds: J.-X. Cheng, X. S. Xie, Taylor & Francis Group, LLC (2013).

[2] M. Dantus, R.M. Bowman, A.H. Zewail, "Femtosecond laser observations of molecular vibration and rotation," Nature, **343,** 737 (1990).

[3] S.A. Malinovskaya, "Observation and control of molecular motion using ultrafast laser pulses," In: Trends in Chemical Physics Research, Editor: A.N. Linke, Nova Science Publishers, Inc. ISBN 1-59454-483-2, pp. 257-280 (2005).

[4] S.A. Malinovskaya, "Chirped pulse control methods for imaging of biological structure and dynamics," I.J. Quant. Chem., **107,** 3151 (2007).

[5] S. A. Malinovskaya, "Mode selective excitation using ultrafast chirped laser pulses", Phys. Rev. A. **73,** 033416 (2006).

[6] H. Zhu, Y. Li, S. Vdović, S. Long, G. He, Q. Guo, "Femtosecond coherent anti-Stokes Raman scattering spectroscopy of hydrogen bonded structure in water and aqueous solutions", Spectrochimica Acta Part A: Mol. and Biomol. Spectr., **151,** 262 (2015).

[7] M. Lindley, K. Hiramatsu, H. Nomoto, F. Shibata, T. Takeshita, S. Kawano, K. Goda, "Ultrafast Simultaneous Raman-Fluorescence Spectroscopy", Anal. Chem. **24**, 15563 (2019).

[8] C. E. Dedic, T. R. Meyer, J. B. Michael, "Single-shot ultrafast coherent anti-Stokes Raman scattering of vibrational/rotational nonequilibrium," Optica **4,** 563 (2017).

[9] G. Matthäus, S. Demmler, M. Lebugle, F. Küster, J. Limpert, A. Tünnermann, S. Nolte, R. Ackermann, "Ultra-broadband two beam CARS using femtosecond laser pulses", Vibr. Spectroscopy, **85,** 128 (2016).

[10] N. V. Vitanov, A. A. Rangelov, B. W. Shore, and K. Bergmann, "Stimulated Raman adiabatic passage in physics, chemistry, and beyond", Rev. Mod. Phys. **89**, 015006 (2017)

[11] A. Bahari, A. A. Zhdanova, M. Shutova, and A. V. Sokolov "Synthesis of ultrafast waveforms using coherent Raman sidebands", Phys. Rev. A **102**, 013520 (2020)

[12] G. Fumero, C. Schnedermann, G. Batignani, T. Wende, M. Liebel, G. Bassolino, C. Ferrante, S. Mukamel, P. Kukura, and T. Scopigno, "Two-Dimensional Impulsively Stimulated Resonant Raman Spectroscopy of Molecular Excited States", Phys. Rev. X **10**, 011051 (2020).

[13] H. Miller, Z. Zhou, J. Shepherd, A. J. M. Wollman, M. C. Leake, "Single-molecule techniques

in biophysics: a review of the progress in methods and applications", Rep. Prog. Phys. **81** 024601 (2018).

[14] M. T. Bremer, P. J. Wrzesinski, N. Butcher, V. V. Lozovoy, M. Dantus, "Highly selective standoff detection and imaging of trace chemicals in a complex background using single-beam coherent anti-Stokes Raman scattering", Appl. Phys. Lett. **99**, 101109 (2011).

[15] N. Dudovich, D. Oron, Y. Silberberg, "Single-pulse coherently controlled nonlinear Raman spectroscopy and microscopy", Nature **418,** 512 (2002).

[16] P. J. Wrzesinski, H. U. Stauffer, J. B. Schmidt, S. Roy, J. R. Gord, "Single-shot thermometry and OH detection via femtosecond fully resonant electronically enhanced CARS (FREE-CARS)," Opt. Lett. **41**, 2021 (2016).

[17] O. Katz, A. Natan, Y. Silberberg, S. Rosenwaks, "Standoff detection of trace amounts of solids by nonlinear Raman spectroscopy using shaped femtosecond pulses", Appl. Phys. Lett. **92**, 171116 (2008).

[18] T. Koo, S. Chan, A. A. Berlin, "Single-molecule detection of biomolecules by surface-enhanced coherent anti-Stokes Raman scattering," Opt. Lett. **30**, 1024 (2005).

[19] M.O. Scully, M.S. Zubairy, *Quantum Optics,* Cambridge University Press (1997).

[20] M. O. Scully, G. W. Kattawar, R. P. Lucht, T. Opatrny, H. Pilloff, A. Rebane, A. V. Sokolov, M. S. Zubairy, "FAST CARS: Engineering a laser spectroscopic technique for rapid identification of bacterial spores," P. Natl. Acad. Sci. USA **99,** 10994 (2002).

[21] D. Pestov, R. K. Murawski, G. O. Ariunbold, X. Wang, M. C. Zhi, A. V. Sokolov, V. A. Sautenkov, Y. V. Rostovtsev, A. Dogariu, Y. Huang, M. O. Scully, "Optimizing the laser-pulse configuration for coherent Raman spectroscopy," Science **316,** 265 (2007).

[22] C.H.R. Ooi, G. Beadie, G.W. Kattawar, J.F. Reinjes, Y. Rostovtsev, M.S. Zubairy, M.O. Scully, "Theory of femtosecond coherent anti-Stokes Raman backscattering enhanced by quantum coherence for standoff detection of bacterial spores", Phys. Rev. A, **72**, 023807 (2005).

[23] D. Oron, N. Dudovich, D. Yelin, Y. Silberberg, "Narrow-band coherent anti-Stokes Raman signals from broad-band pulses," Phys. Rev. Lett. **88,** 063004 (2002).

[24] D. Oron, N. Dudovich, Y. Silberberg, "Femtosecond phase-and-polarization control for background-free coherent anti-Stokes Raman spectroscopy," Phys. Rev. Lett. **90,** 213902 (2003).

[25] V. V. Lozovoy, B. W. Xu, J. C. Shane, M. Dantus, "Selective nonlinear optical excitation with

pulses shaped by pseudorandom Galois fields," Phys. Rev. A **74,** 041805(R) (2006).

[26] H. Li, D.A. Harris, B. Xu, P.J. Wrzesinski, V.V. Lozovoy, M. Dantus, "Coherent mode-selective Raman excitation towards standoff detection," Opt. Expr. **16,** 5499 (2008).

[27] S. R. Oh, J. H. Park, K. Kim, J. Y. Lee, S. Kim, "Multiplex CARS imaging with spectral notch shaped laser pulses delivered by optical fibers," Opt. Express **25**, 32178 (2017).

[28] D. R. Richardson, H. U. Stauffer, S. Roy, J. R. Gord, "Comparison of chirped-probe-pulse and hybrid femtosecond/picosecond coherent anti-Stokes Raman scattering for combustion thermometry," Appl. Opt. **56**, E37 (2017).

[29] A. Konar, V. V. Lozovoy, M. Dantus, "Stimulated Emission Enhancement Using Shaped Pulses", J. Phys. Chem. A **120,** 2002 (2016).

[30] D. Pestov, X. Wang, R. K. Murawski, G. O. Ariunbold, V. A. Sautenkov, A. V. Sokolov, "Pulse shaping for mode-selective ultrafast coherent Raman spectroscopy of highly scattering solids," J. Opt. Soc. Am. B **25,** 768 (2008).

[31] A. M. D. Thomasen, T. Mukai, and T. Byrnes, "Ultrafast coherent control of spinor Bose-Einstein condensates using stimulated Raman adiabatic passage". Phys. Rev. A **94**, 053636 (2016).

[32] T. Hellerer, A. M. K. Enejder, A. Zumbusch, "Spectral focusing: High spectral resolution spectroscopy with broad-bandwidth laser pulses," Appl. Phys. Lett. **85,** 25 (2004).

[33] R. M. Onorato, N. Muraki, K. P. Knutsen, R. J. Saykally, "Chirped coherent anti-Stokes Raman scattering as a high-spectral and spatial resolution microscopy," Opt. Lett. **32,** 2858 (2007).

[34] R. Glenn, M. Dantus, "Single broadband phase-shaped pulse stimulared Raman spectroscopy for standoff trace explosive detection," J. Phys. Chem. Lett. **7,** 117 (2016).

[35] J. X. Cheng, A. Volkmer, X. S. Xie, "Theoretical and experimental characterization of coherent anti-Stokes Raman scattering microscopy," J. Opt. Soc. Am. B **19,** 1363 (2002).

[36] N. Pandya, G. Liu, F. A. Narducci, J. Chathanathil, S. Malinovskaya, " Creation of the maximum coherence via adiabatic passage in the four-wave mixing process of coherent anti-Stokes Raman scattering," Chem. Phys. Lett. **738,** 136763 (2020).

[37] M. Sukharev, A. Nitzan, "Optics of exciton-plasmon nanomaterials", J. Phys.: Condens. Matter **29,** 443003 (2017).

[38] H. Fujisaki, J. E. Straub, "Vibrational energy relaxation in proteins", Proc. Natl. Acad. Sci.

**102,** 6726 (2005).

[39] S. Malinovskaya, "Prevention of decoherence by two femtosecond chirped pulse trains", Opt. Lett. **33,** 2245 (2008).

[40] B. J. Berne, M. Borkovec, J. E. Straub, "Classical and modern methods in reaction rate theory", J. Phys. Chem. **92,** 3711 (1988).

[41] M. Gruebele, P. G. Wolynes, "Vibrational energy flow and chemical reactions", Acc. Chem. Res. **37,** 261 (2004).

[42] B. C. Dian, A. Longarte, T. S. Zwier, "Conformational dynamics in a dipeptide after single-mode vibrational excitation", Science **296,** 2369 (2002).

[43] W. D. Gillespie, S. P. Sharma, "Raman scattering measurements of vibrational relaxation in expanding nitrogen", In: R. Brun, L. Z. Dumitrescu (eds) Shock Waves @ Marseille II. Springer, Berlin, Heidelberg. https://doi.org/10.1007/978-3-642-78832-1_38.

[44] M. Yasuhisa, K. Teizo, "Vibrational energy relaxation of metalloporphyrins in a condensed phase probed by time-resolved resonance Raman spectroscopy", Bulletin Chem. Soc. Japan **75,** 623 (2002), https://doi.org/10.1246/bcsj.75.623.

[45] E. S. Manuilovich, V. A. Astapenko, P. A. Golovinskiia, "Propagation of Ultrashort Laser Pulses in Dry and Humid Air", Atmosph. Ocean. Opt., **28,** 209 (2015).

[46] P. Sprangle, J. R. Peñano, B. Hafizi, "Propagation of intense short laser pulses in the atmosphere," Phys. Rev. E, **66**, 046418 (2002).

[47] *Analytical Chemistry: An Introduction*, (Saunders Golden Sunburst Series) 7th Ed., by D. A. Skoog, D. M. West, F. J. Holler (1999).

[48] R. Sabatini, M. Richardson, "New techniques for laser beam atmospheric extinction measurements from manned and unmanned aerospace vehicles" Cent. Eur. J. Eng, **3,** 11 (2013).

[49] Y. LeCun, Y. Bengio, G. Hinton, "Deep learning," Nature **521,** 436 (2015).

[50] O. Simeone, " A Brief Introduction to Machine Learning for Engineers," arXiv:1709.02840 [cs.LG] (2018).

[51] D. M. Hawkins, "The Problem of Overfitting" Journal of Chemical Information and Computer Sciences **44 (1)**, 1-12 (2004).

[52] D. Goswami, "Laser Phase Modulation Approaches towards Ensemble Quantum Computing", Phys. Rev. Lett. **88**, 177901 (2002).

[53] G. Liu, S. A. Malinovskaya, "Creation of ultracold molecules within the lifetime scale by direct

implementation of an optical frequency comb," J. Mod. Opt., **65**, 1309 (2018).

[54] D. P. Kingma, J. Ba, "Adam: A Method for Stochastic Optimization", arXiv:1412.6980 (2014).

[55] R. Caruana, S. Lawrence, C. L. Giles, "Overfitting in neural nets: Backpropagation, conjugate gradient, and early stopping", In *Advances in Neural Information Processing Systems 13 - Proc. 2000 Conf.* (2001).

[56] N. V. Vitanov, K.-A. Suominen, B. W. Shore, "Creation of coherent atomic superpositions by fractional stimulated Raman adiabatic passage", J. Phys. B: At. Mol. Opt. Phys. **32,** 4535 (1999).

[57] G. Liu, F. A. Narducci, S. A. Malinovskaya, "Limits to remote molecular detection via coherent anti-Stokes Raman spectroscopy using a maximal coherence control technique," J. Mod. Opt. **67,** 21-25 (2020).

[58] V. Nair, G. Hinton, "Rectified Linear Units Improve Restricted Boltzmann Machines," In *Proc. of the 27th Intern. Conf. on Machine Learning,* Haifa, Israel (2010).

[59] K. He, X. Zhang, S. Ren, J. Sun, "Delving Deep into Rectifiers: Surpassing Human-Level Performance on ImageNet Classification," arXiv:1502.01852 (2015).